Spin anisotropy effects in dimer single molecule magnets

Dmitri V. Efremov[1,*] and Richard A. Klemm[2,†]
[1]*Institut für Theoretische Physik, Technische Universität Dresden, D-01062 Dresden, Germany*
[2]*Department of Physics, Kansas State University, Manhattan, Kansas 66506, USA*
(Received 25 January 2006; revised manuscript received 30 June 2006; published 15 August 2006)

We present a model of homoionic, equal-spin s_1 dimer single molecule magnets exhibiting D_{2h}, C_{2v}, or S_2 molecular group symmetry, focusing upon the simplest D_{2h} case. The spins within each dimer interact via the Heisenberg and the most general set of four quadratic anisotropic spin interactions with respective strengths J and $\{J_j\}$, and with the magnetic induction $\boldsymbol{B}$. We solve the model exactly for $s_1=1/2$, and analytically for $\boldsymbol{B}$ along the crystal directions and numerically for other $\boldsymbol{B}$ directions for $s_1=1$ and 5/2, and present $\boldsymbol{M}(\boldsymbol{B})$ curves at low T for these cases with antiferromagnetic Heisenberg couplings ($J<0$). Low-T $C_V(\boldsymbol{B})$ curves for $s_1=1/2$ and electron paramagnetic susceptibility $\chi(\boldsymbol{B},\omega)$ for $s_1=1$ are also provided. For weakly anisotropic dimers, the Hartree approximation, or strong exchange limit, yields rather simple analytic formulas for $\boldsymbol{M}(\boldsymbol{B})$ and $C_V(\boldsymbol{B})$ at arbitrary s_1 that accurately fit the exact solutions at sufficiently low T or large B. Low-T, large-B formulas for the inelastic neutron-scattering cross section $S(\boldsymbol{B},\boldsymbol{q},\omega)$ and $\chi(\boldsymbol{B},\omega)$ with arbitrary s_1 and $\boldsymbol{B}$ in the Hartree approximation are also given. For antiferromagnetic Heisenberg couplings ($J<0$) and weak anisotropy interactions ($|J_j/J|\ll 1$), we provide analytic formulas for the $2s_1$ level-crossing magnetic inductions $B^{\rm lc}_{s,s_1}(\theta,\phi)$, at which the low-$T$ magnetization $\boldsymbol{M}(\boldsymbol{B})$ exhibits steps and the low-T specific heat $C_V(\boldsymbol{B})$ exhibits zeroes, surrounded by double peaks of uniform height. Strong anisotropy interactions drastically alter these behaviors, however. Our results are discussed with regard to existing experiments on $s_1=5/2$ Fe_2, $s_1=3/2$ Cr_2, and $s_1=1$ Ni_2 dimers, suggesting the presence of single-ion anisotropy in three of them, but apparently without any sizeable anisotropic exchange interactions. Further experiments on single crystals of these and higher-spin dimers are therefore warranted, and we particularly urge further electron paramagnetic resonance and inelastic neutron-scattering experiments to be performed.

DOI: 10.1103/PhysRevB.74.064408 PACS number(s): 75.10.Jm, 75.75.+a

I. INTRODUCTION

Single molecule magnets (SMM's) have been under intense study recently, due to their potential uses in magnetic storage and quantum computing.[1–3] The materials consist of insulating crystalline arrays of identical SMM's 1–3 nm in size, each containing two or more magnetic ions. Since the magnetic ions in each SMM are surrounded by nonmagnetic ligands, the intermolecular magnetic interactions are usually negligible. Although the most commonly studied SMM's are the high-spin Mn_{12} and Fe_8,[1–5] such SMM's contain a variety of ferromagnetic (FM) and antiferromagnetic (AFM) intramolecular interactions, rendering unique fits to a variety of experiments difficult.[6]

In addition, there have been many studies of AFM Fe_n ring compounds, where $n=6,8,10,12$, etc., and of the ring compound Cr_8.[7–16] In these studies, analyses of inelastic neutron-scattering (INS) and electron paramagnetic resonance (EPR) data, and the magnetic induction $\boldsymbol{B}$ dependence of the low-temperature T specific-heat C_V and magnetization $\boldsymbol{M}$ steps were made, using the isotropic Heisenberg near-neighbor exchange interaction, the Zeeman interaction, and various near-neighbor exchange and axial single-ion anisotropy interactions.[7–18] However, the rings were so complicated that analyses of the data using those simple models were inaccessible to present day computers.[8,9] Thus some of those authors used either numerical evaluations, simulations, or phenomenological fits to a first-order perturbation expansion with different spin anisotropy values for each total ring spin value.[8–10,17,18] None of those authors studied the effects of azimuthal single-ion anisotropy.

Here we focus on the much simpler cases of equal spin $s_1=s_2$ magnetic dimers exhibiting D_{2h} molecular group symmetry, for which some of the spin anisotropy effects can be evaluated analytically, and many other effects can be investigated in detail numerically, and compared with experiment. Extensions to the lower C_{2v} and S_2 symmetries are straightforward, and some of our results also apply to those cases. AFM dimers with $s_1=1/2$, 1, 3/2,[19–26] various forms of Fe_2 with $s_1=5/2$,[13,27–32] and both FM and weakly coupled AFM Gd_2 dimers with $s_1=7/2$ have been studied recently.[33–35] Several Fe_2 dimers and effective $s_1=9/2$ dimers of the type $[Mn_4]_2$ (Refs. 36–38) have magnetic interactions weak enough that their effects can be probed at $T\approx 1$ K with presently available $\boldsymbol{B}$. Recent measurements showed that in some of those systems, the total spin anisotropy of the Mn_4 monomers in the ground state $s_1=9/2$ manifold was found to be much stronger than the intermonomer Heisenberg interaction.[38] However, the zero-field splittings of the triplet states observed in INS studies of the Ni spin chains, $Ni(C_5D_{14}N_2)_2$-$N_3(PF_6)$ and $Ni(C_9H_{24}N_4)(NO_2)ClO_4$, have provided direct measurements of both the axial and azimuthal single-ion anisotropy interactions in those materials.[39–43] A comparison of our results with $\boldsymbol{M}(\boldsymbol{B})$ step data on a Fe_2 and both $\boldsymbol{M}(\boldsymbol{B})$ step data and INS data on a Ni_2 dimer strongly suggests a substantial presence of axial and/or azimuthal single-ion spin anisotropy, without appreciable anisotropic exchange interactions.[23,29]

The paper is organized as follows. In Sec. II, we present the model in the crystal representation and give exact formulas for the matrix elements. The general thermodynamics are

presented in Sec. III, along with the universal $M(B)$ and $C_V(B)$ behavior associated with the energy-level crossing. In Sec. IV, we present our induction representation results for the eigenstates to first order in the anisotropy energies. We also give the level-crossing inductions $B^{\rm lc}_{s,s_1}(\theta,\phi)$ to second order in the anisotropy interactions. In Sec. V, we solve the model exactly for $s_1=1/2$, and give plots and analytic expressions for $\boldsymbol{M}$, the specific heat C_V, and $B^{\rm lc}_{1,1/2}(\theta,\phi)$ for $\boldsymbol{B}\|\hat{\boldsymbol{x}},\hat{\boldsymbol{y}},\hat{\boldsymbol{z}}$, along a crystal axis direction. In Sec. VI, we discuss the exact solution for $s_1=1$ for those $\boldsymbol{B}$ directions, and give examples of the low-T $\boldsymbol{M}(\boldsymbol{B})$ and $B^{\rm lc}_{s,1}(\theta,\phi)$ curves. We also present examples of the low-T $s_1=5/2$ $\boldsymbol{M}(\boldsymbol{B})$ and $B^{\rm lc}_{s,5/2}(\theta,\phi)$ curves for $s=1,2,3$. In Sec. VII, we present the asymptotic Hartree (or strong exchange limit) expressions for the thermodynamic quantities $\boldsymbol{M}$ and C_V, and for the INS cross section $S(\boldsymbol{B},\boldsymbol{q},\omega)$ and the EPR susceptibility $\chi(\boldsymbol{B},\omega)$ for arbitrary s_1, that are accurate at sufficiently low T and/or large B. In Sec. VIII, we discuss examples of strong anisotropy interactions for $s_1=1/2$, $5/2$. Finally, in Sec. IX, we summarize our results and discuss them with regard to existing experiments on the dimers, $Na_2Ni_2(C_2O_4)_3(H_2O)_2$,[23] $Cs_3Cr_2Br_2$,[24] μ-oxalatotetrakis(acetylacetonato) Fe_2,[28] and $[Fe(salen)Cl]_2$, where salen is N,N'-ethylenebis(salicylideneiminato).[29]

II. MODEL IN THE CRYSTAL REPRESENTATION

We represent the $s_1=s_2$ dimer quantum states, $|\psi_s^m\rangle$ in terms of the total (or global) spin and magnetic quantum numbers s and m, where $\boldsymbol{S}=\boldsymbol{S}_1+\boldsymbol{S}_2$ and $S_z=\boldsymbol{S}\cdot\hat{\boldsymbol{z}}$ satisfy $\boldsymbol{S}^2|\psi_s^m\rangle=s(s+1)|\psi_s^m\rangle$ and $S_z|\psi_s^m\rangle=m|\psi_s^m\rangle$, where $s=0,1,\ldots,2s_1$, $m=-s,\ldots,s$, and we set $\hbar=1$. We also have $S_\pm|\psi_s^m\rangle=A_s^{\pm m}|\psi_s^{m\pm1}\rangle$,where $S_\pm=S_x\pm iS_y$ and

$$A_s^m=\sqrt{(s-m)(s+m+1)}. \tag{1}$$

For an arbitrary $\boldsymbol{B}$, we assume the Hamiltonian has the form $\mathcal{H}=\mathcal{H}_0+\mathcal{H}_a+\mathcal{H}_c+\mathcal{H}_e+\mathcal{H}_f$, where

$$\mathcal{H}_0=-J\boldsymbol{S}^2/2-\gamma\boldsymbol{S}\cdot\boldsymbol{B} \tag{2}$$

contains the Heisenberg exchange and Zeeman interactions, the gyromagnetic ratio $\gamma=g\mu_B$, $g\approx2$ and μ_B is the Bohr magneton.

An homoionic dimer with symmetric ligands consisting of equal spins exhibiting molecular group $g=D_{2h}$ (Fig. 1), C_{2v}, or S_2 (also Fig. 1) symmetry has either a center of inversion or sufficient mirror planes,[44,45] so that Dzyaloshinskii-Moriya (DM) interactions do not arise.[46,47] For simplicity, we focus upon the D_{2h} case.

For $g=D_{2h}$, the single-ion axial and azimuthal anisotropy terms, which may be written in terms of the molecular coordinates $(\hat{\boldsymbol{x}},\hat{\boldsymbol{y}},\hat{\boldsymbol{z}})$,

$$\mathcal{H}_a=-J_a\sum_{i=1}^{2}S_{iz}^2 \tag{3}$$

and

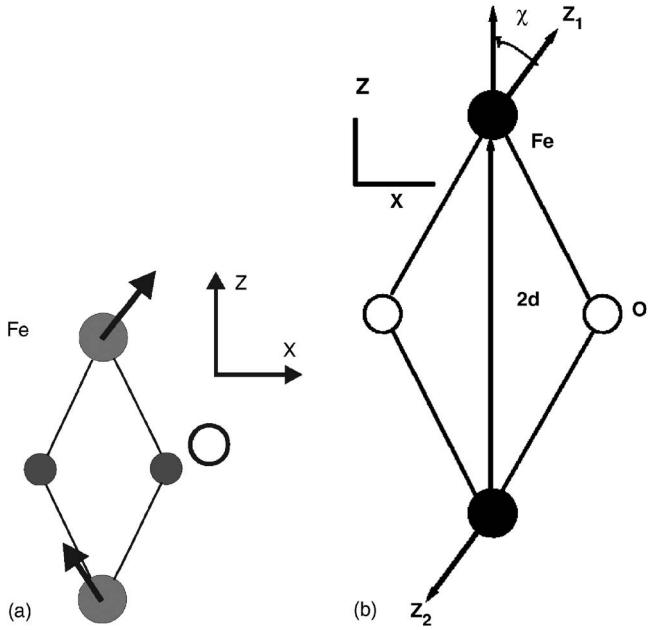

FIG. 1. Left: Sketch of an Fe_2 dimer with D_{2h} molecular group symmetry containing a di-μ oxo bridge, with two bridging O^{-2} ions (O). The arrows represent spins. Right: Fe_2 dimer with S_2 molecular group symmetry. Ligands (not pictured) are attached to the Fe^{+3} ions (Fe), leading to the easy axis along $\hat{\boldsymbol{z}}_1=-\hat{\boldsymbol{z}}_2$ (arrows), which is at an angle χ from the dimer axis $\boldsymbol{d}$.

$$\mathcal{H}_e=-J_e\sum_{i=1}^{2}(S_{ix}^2-S_{iy}^2), \tag{4}$$

respectively, arise from spin-orbit interactions of the local crystal field with the individual spins. We take the laboratory z axis parallel to the dimer axis $\hat{\boldsymbol{d}}$ for all symmetries, as pictured in Fig. 1. For $g=C_{2v},S_2$, the principal axes $\hat{\boldsymbol{z}}_1=-\hat{\boldsymbol{z}}_2$, etc., are rotated with respect to the dimer axis. $\mathcal{H}_a$ has the same form as Eq. (3) with respect to the (rotated) axial principal axis, but $\mathcal{H}_e$ is slightly different from Eq. (4), as discussed in Appendix A. The azimuthal anisotropy term has usually been neglected in the SMM literature. However, the axial anisotropy term has been studied with regard to complexes containing a single magnetic ion, such as Ni^{+2},[48] in one example of an unequal-spin dimer,[49] in which the expected DM interactions were also omitted, and in clusters and chains of larger numbers of identical magnetic ions.[23–25,39–41,48,50,51] Azimuthal single-ion anisotropy was directly observed in two Ni chain compounds and anticipated in $Cs_3Cr_2Br_2$.[24,40,41]

For $g=D_{2h}$, the local axially and azimuthally anisotropic spin-spin interactions are

$$\mathcal{H}_f=-J_fS_{1z}S_{2z}, \tag{5}$$

$$\mathcal{H}_c=-J_c(S_{1x}S_{2x}-S_{1y}S_{2y}). \tag{6}$$

It is common to combine the effects of the single-ion and anisotropic exchange interactions into the effective total spin axial and azimuthal anisotropy terms,

$$\mathcal{H}_b = -J_b S_z^2 \tag{7}$$

and

$$\mathcal{H}_d = -J_d(S_x^2 - S_y^2), \tag{8}$$

respectively, which only depend upon the components of the total spin $\boldsymbol{S}$. Equations (7) and (8) constitute an effective anisotropy Hamiltonian that operates within a fixed s group of substates, and these and their generalizations to quartic order have been very successful in providing fits to experimental data.[5,36,46] They arise when the tensor total spin interaction with a fixed spin quantum number s has the form $\boldsymbol{S}\cdot\vec{\boldsymbol{\Lambda}}\cdot\boldsymbol{S}$, resulting in the principal axes x, y, and z,[46,48] as pictured for D_{2h} symmetry in the left panel of Fig. 1. Then $J=-(\Lambda_{xx}+\Lambda_{yy})/2$, $J_b=-\Lambda_{zz}+(\Lambda_{xx}+\Lambda_{yy})/2$, and $J_d=(\Lambda_{yy}-\Lambda_{xx})/2$. Taking $|J_d/J|\ll 1$ and $|J_b/J|\ll 1$ still leaves J_d/J_b unrestricted.

However, fits to different experiments on the same sample often require different parametrization sets $\{J_{b,\tilde{s}}, J_{d,\tilde{s}}, \ldots\}$ for each experimentally attainable set of sets labeled by $\tilde{s}$.[52] Since the nominal total spin quantum number s is not always a good quantum number in many experiments, $\tilde{s}$ does not always have a one-to-one correspondence to s, so that the combined number of parameters required to fit all possible data on a single material often can be very large. Here we study the simplest SMM systems, in which a small set of parameters is capable of describing all of the possible experiments on a given material.

For dimers with D_{2h} symmetry, these effective Hamiltonian terms satisfy

$$2\mathcal{H}_f/J_f = \mathcal{H}_b/J_b - \mathcal{H}_a/J_a, \tag{9}$$

$$2\mathcal{H}_c/J_c = \mathcal{H}_d/J_d - \mathcal{H}_e/J_e, \tag{10}$$

so we need only include either $\mathcal{H}_a$ or $\mathcal{H}_f$ and $\mathcal{H}_e$ or $\mathcal{H}_c$, respectively.[48,49] For $g=C_{2v}$, $\mathcal{H}_f$ and $\mathcal{H}_c$ have the same forms as in Eqs. (5) and (6), but S_2 symmetry leads to a different axial principle axis for $\mathcal{H}_f$, and a slightly different $\mathcal{H}_c$ form from Eq. (6), as discussed in Appendix A. Since $\mathcal{H}_a$ and $\mathcal{H}_e$ describe the axial and azimuthal anisotropy each single ion attains from its surrounding environment, and $\mathcal{H}_c$ and $\mathcal{H}_f$ arise from dipole-dipole and anisotropic exchange interactions, they are the physically relevant local anisotropy interactions. We therefore choose $\mathcal{H}=\mathcal{H}_0+\mathcal{H}_a+\mathcal{H}_c+\mathcal{H}_e+\mathcal{H}_f$. We denote $\mathcal{H}_f$ and $\mathcal{H}_c$ the axial and azimuthal anisotropic exchange interactions, even though they sometimes contain larger dipole-dipole contributions. Here we focus upon the simplest D_{2h} symmetry, for which the principle axes of the single-ion and anisotropic exchange interactions coincide, but many of our results can be generalized to the lower C_{2v} and S_2 symmetries.

Practically, we may make use of the simpler $\tilde{\mathcal{H}}=\mathcal{H}_0+\tilde{\mathcal{H}}_a+\tilde{\mathcal{H}}_b+\tilde{\mathcal{H}}_d+\tilde{\mathcal{H}}_e$ by letting $J_a\to J_a-J_f/2$, $J_b\to J_f/2$, $J_d\to J_c/2$, and $J_e\to J_e-J_c/2$ in $\tilde{\mathcal{H}}_a$, $\tilde{\mathcal{H}}_b$, $\tilde{\mathcal{H}}_d$, and $\tilde{\mathcal{H}}_e$, respectively. We note that $\mathcal{H}_b$, $\mathcal{H}_f$, and $\mathcal{H}_a$ are symmetric under $\hat{\boldsymbol{x}}\leftrightarrow\hat{\boldsymbol{y}}$, whereas $\mathcal{H}_d$, $\mathcal{H}_c$, and $\mathcal{H}_e$ are antisymmetric under $\hat{\boldsymbol{x}}\leftrightarrow\hat{\boldsymbol{y}}$, independent of s_1.

For the case of the many Fe_2 SMM's containing a di-μ oxo bridge,[27] some of which are constituents of the high-spin SMM Fe_8 and the AFM Fe_n rings,[4,8,9] the exchange between the Fe^{+3} $s_1=5/2$ spins occurs via two oxygen ions, and these four ions essentially lie in the same (xz) plane.[13,27] For $g=D_{2h}$, we set the z axis parallel to the dimer axis, as pictured in the left panel of Fig. 1. The azimuthal axes are perpendicular to the easy axis, satisfying $\hat{\boldsymbol{x}}\times\hat{\boldsymbol{y}}=\hat{\boldsymbol{z}}$. In $[\mathrm{Fe(salen)Cl}]_2$, the Cl^- ions are positioned off the dimer axis,[29] as pictured in the right panel of Fig. 1, so the molecule exhibits S_2 symmetry. This leads to complications arising from the different single-ion and anisotropic exchange principle axes, as discussed in Appendix A.

We generally expect each of the J_j for $j=a,c,e,f$ to satisfy $|J_i/J|\ll 1$, but there are not generally any other restrictions upon the various magnitudes of the J_j. Since most dimers studied to date have predominantly AFM couplings $(J<0)$, and also because their magnetizations and specific heats are particularly interesting, we shall only consider AFM dimers. For simplicity, we only treat homoionic, equal-spin $s_1=s_2$ dimers with equivalent ligand groups exhibiting molecular group symmetry S_2, C_{2v}, or D_{2h}, so that DM interactions do not occur.[46–48] Hence our Hamiltonian $\mathcal{H}$ is the most general quadratic anisotropic spin Hamiltonian of an equal-spin dimer with S_2 or higher molecular group symmetry. Nonhomoionic, unequal-spin dimers were discussed elsewhere.[46,49,53]

For $\boldsymbol{B}=B(\sin\theta\cos\phi, \sin\theta\sin\phi, \cos\theta)$, we have

$$\mathcal{H}_0|\psi_s^m\rangle = E_s^m|\psi_s^m\rangle + \delta E\sum_{\sigma=\pm1} e^{-i\sigma\phi}A_s^{\sigma m}|\psi_s^{m+\sigma}\rangle, \tag{11}$$

$$\tilde{\mathcal{H}}_b|\psi_s^m\rangle = -\frac{J_f}{2}m^2|\psi_s^m\rangle, \tag{12}$$

and

$$\tilde{\mathcal{H}}_d|\psi_s^m\rangle = \frac{-J_c}{4}\sum_{\sigma=\pm1} F_s^{\sigma m}|\psi_s^{m+2\sigma}\rangle, \tag{13}$$

where

$$E_s^m = -Js(s+1)/2 - mb\cos\theta, \tag{14}$$

$$\delta E = -\frac{1}{2}b\sin\theta, \tag{15}$$

$$b = \gamma B, \tag{16}$$

and

$$F_s^{\sigma m} = A_s^{\sigma m}A_s^{1+\sigma m}. \tag{17}$$

$\mathcal{H}_a$ and $\mathcal{H}_c$ contain the individual spin operators S_{iz} and $S_{i\pm}$ for $i=1,2$. A compact form for the single-ion operations for arbitrary (s_1,s,m) is

$$S_{i\pm}|\psi_s^m\rangle = \frac{1}{2}A_s^{\pm m}|\psi_s^{m\pm1}\rangle \mp \frac{1}{2}(-1)^i(C_{s,s_1}^{\pm m}|\psi_{s-1}^{m\pm1}\rangle - C_{s+1,s_1}^{-1\mp m}|\psi_{s+1}^{m\pm1}\rangle), \tag{18}$$

$$S_{iz}|\psi_s^m\rangle = \frac{m}{2}|\psi_s^m\rangle - \frac{1}{2}(-1)^i(D_{s,s_1}^m|\psi_{s-1}^m\rangle + D_{s+1,s_1}^m|\psi_{s+1}^m\rangle), \tag{19}$$

where

$$C_{s,s_1}^m = \eta_{s,s_1}\sqrt{(s-m)(s-m-1)}, \tag{20}$$

$$D_{s,s_1}^m = \eta_{s,s_1}\sqrt{(s^2-m^2)}, \tag{21}$$

and

$$\eta_{s,s_1} = \sqrt{[(2s_1+1)^2-s^2]/(4s^2-1)}. \tag{22}$$

Single-spin matrix elements derived from these equations contain the second-order projection coefficients,[49] in this case η_{s,s_1}, which were presented by Bencini and Gatteschi and later by Boča,[46,53] who showed their analogy to the off-diagonal Landé magnetization. However, to our knowledge, no plots of the separate effects of single-ion or anisotropic exchange interactions have been published.[53] The important point is that many of the extremely simple results obtained in the following from these simple, compact equations for the equal-spin dimer with $s_1>1/2$ lead to previously unknown, interesting single-ion anisotropy effects, some of which have been observed experimentally, but their significance has not been appreciated or understood. In addition, these simple results can be readily generalized to at least four arbitrary spins. Boča presented most of the analogous coefficients for three and four spins.[53] Using the Schwinger boson technique, we have independently derived these simple second-order projection coefficients and their generalizations to the analogous, although increasingly complex, analytic forms for two, three, and four arbitrary spins.[54] This has already been done for tetramers with T_d, D_{2d}, S_4, and C_{4v} symmetries,[55] and is currently in progress for C_{3v} or lower-symmetry tetramers,[54] which might provide a better fit to $\{Ni_4Mo_{12}\}$,[50] $CrNi_3$,[56] and the low-symmetry Mn_4 compounds.[57]

For $s=0$, we require $m=0$, for which $C_{0,s_1}^0=D_{0,s_1}^0=0$. We then find

$$\tilde{\mathcal{H}}_a|\psi_s^m\rangle = \frac{J_f-2J_a}{4}\left(G_{s,s_1}^m|\psi_s^m\rangle + \sum_{\sigma'=\pm1} H_{s,s_1}^{m,\sigma'}|\psi_{s+2\sigma'}^m\rangle\right), \tag{23}$$

$$\tilde{\mathcal{H}}_e|\psi_s^m\rangle = \frac{J_c-2J_e}{8}\sum_{\sigma=\pm1}\left(L_{s,s_1}^{\sigma m}|\psi_s^{m+2\sigma}\rangle + \sum_{\sigma'=\pm1} K_{s,s_1}^{\sigma m,\sigma'}|\psi_{s+2\sigma'}^{m+2\sigma}\rangle\right), \tag{24}$$

$$G_{s,s_1}^m = m^2 + (D_{s,s_1}^m)^2 + (D_{s+1,s_1}^m)^2 = s(s+1) - 1 + [2m^2+1-2s(s+1)]\alpha_{s,s_1}, \tag{25}$$

$$H_{s,s_1}^{m,\sigma'} = D_{s+(\sigma'+1)/2,s_1}^m D_{s+(3\sigma'+1)/2,s_1}^m, \tag{26}$$

$$K_{s,s_1}^{x,\sigma'} = C_{s+(\sigma'+1)/2,s_1}^{-\sigma' x-(1+\sigma')/2} C_{s+(3\sigma'+1)/2,s_1}^{-\sigma' x-(3\sigma'+1)/2}, \tag{27}$$

$$L_{s,s_1}^x = 2F_s^x\alpha_{s,s_1}, \tag{28}$$

and

$$\alpha_{s,s_1} = \frac{3s(s+1)-4s_1(s_1+1)-3}{(2s-1)(2s+3)}. \tag{29}$$

We note that $2\alpha_{s,s_1}=1-\eta_{s,s_1}^2-\eta_{s+1,s_1}^2$ and that Eq. (29) holds for $s\geq 0$. Equations (18) and (19) allow for an exact expression of the most general Hamiltonian matrix of arbitrary order in the individual spin operators, and for $s_1=1/2$, an exact solution of the resulting eigenvalues.

In the crystal representation, the operations of $\mathcal{H}_0$, $\tilde{\mathcal{H}}_b$, and $\tilde{\mathcal{H}}_d$ satisfy the selection rules $\Delta s=0$, $\Delta m=0,\pm1,\pm2$. The local anisotropy interactions $\tilde{\mathcal{H}}_a$ and $\tilde{\mathcal{H}}_e$ allow transitions satisfying $\Delta s=0,\pm2$, $\Delta m=0$, and $\Delta s=0,\pm2$, $\Delta m=\pm2$, respectively, so in the presence of $\tilde{\mathcal{H}}_a$ and/or $\tilde{\mathcal{H}}_e$, s is no longer a good quantum number, unless $s_1=1/2$.

III. GENERAL THERMODYNAMICS

In order to obtain the thermodynamic properties, we first calculate the canonical partition function, $Z=\mathrm{Tr}\exp(-\beta\mathcal{H})$. Since $\mathcal{H}$ is not diagonal in the (s,m) representation, we must construct the wave function from all possible spin states. We then write

$$Z = \mathrm{Tr}\langle\Psi_{s_1}|e^{-\beta\mathcal{H}}|\Psi_{s_1}\rangle, \tag{30}$$

where $|\Psi_{s_1}\rangle$ is constructed from the $\{|\psi_s^m\rangle\}$ basis as

$$\langle\Psi_{s_1}| = (\langle\psi_{2s_1}^{2s_1}|,\langle\psi_{2s_1}^{2s_1-1}|,\ldots,\langle\psi_1^0|,\langle\psi_1^{-1}|,\langle\psi_0^0|), \tag{31}$$

where $\beta=1/(k_BT)$ and k_B is Boltzmann's constant. To evaluate the trace, it is useful to diagonalize the $\langle\Psi_{s_1}|\mathcal{H}|\Psi_{s_1}\rangle$ matrix. To do so, we let $|\Psi_{s_1}\rangle=\boldsymbol{U}|\Phi_{s_1}\rangle$, where

$$\langle\Phi_{s_1}| = (\langle\phi_{n_{s_1}}|,\langle\phi_{n_{s_1}-1}|,\ldots,\langle\phi_1|), \tag{32}$$

is constructed from the new orthonormal basis $\{|\phi_n\rangle\}$, and $\boldsymbol{U}$ is a unitary matrix of rank $n_{s_1}=(2s_1+1)^2$. Choosing $\boldsymbol{U}$ to diagonalize $\mathcal{H}$, $U\mathcal{H}U^\dagger=\tilde{\mathcal{H}}$, we generally obtain $\tilde{\mathcal{H}}|\phi_n\rangle=\epsilon_n|\phi_n\rangle$ and the partition function for a SMM dimer,

$$Z = \sum_{n=1}^{n_{s_1}}\exp(-\beta\epsilon_n). \tag{33}$$

The specific heat $C_V=k_B\beta^2\partial^2\ln Z/\partial\beta^2$ is then easily found at all $T,\boldsymbol{B}$,

$$C_V = \frac{k_B\beta^2}{Z^2}\left[Z\sum_{n=1}^{n_{s_1}}\epsilon_n^2e^{-\beta\epsilon_n} - \left(\sum_{n=1}^{n_{s_1}}\epsilon_ne^{-\beta\epsilon_n}\right)^2\right]. \tag{34}$$

The magnetization

$$\boldsymbol{M} = -\frac{1}{Z}\sum_{n=1}^{n_{s_1}}\boldsymbol{\nabla}_{\boldsymbol{B}}(\epsilon_n)\exp(-\beta\epsilon_n) \tag{35}$$

requires $\boldsymbol{\nabla}_{\boldsymbol{B}}(\epsilon_n)$ for each $\boldsymbol{B}$. As $T\to0$, at most two eigenstates are relevant. For most B values, only one ϵ_n is important. But

near the reduced sth level-crossing induction $b_s^* = \gamma B_{s,s_1}^{\rm lc}(\theta,\phi)$ at which $\epsilon_s = \epsilon_{s-1}$, two eigenstates are relevant. We then obtain for these two energies

$$C_V(b)/k_B \approx \frac{(\beta\Delta\epsilon_s/2)^2}{\cosh^2(\beta\Delta\epsilon_s/2)}, \tag{36}$$

$$M(b) \approx \frac{1}{2}(M_s + M_{s-1}) + \frac{1}{2}(M_s - M_{s-1})\tanh(\beta\Delta\epsilon_s/2), \tag{37}$$

where

$$\Delta\epsilon_s = \epsilon_s(b) - \epsilon_{s-1}(b), \tag{38}$$

and $M_s = \gamma\nabla_b\epsilon_s(b)$ is the magnetization of the sth eigenstate only. We then expand in powers of $b-b_s^*$,

$$\epsilon_s(b) = \epsilon_s(b_s^*) + (b-b_s^*)a_{1,s} + \frac{1}{2}(b-b_s^*)^2 a_{2,s} + \cdots, \tag{39}$$

and we find

$$C_V(b_s^*) \underset{T\to 0}{\to} 0, \tag{40}$$

$$C_V\left(b_s^* \pm \frac{2c}{\beta(a_{1,s}-a_{1,s-1})}\right) \underset{k_BT\ll|J|}{\to} C_V^{\rm peak} \tag{41}$$

$$C_V^{\rm peak}/k_B = \left(\frac{c}{\cosh c}\right)^2$$

$$\approx 0.439\,229, \tag{42}$$

and

$$M(b_s^*)/\gamma \underset{T\to 0}{\to} \frac{1}{2}(a_{1,s} + a_{1,s-1})$$

$$= s - 1/2 + \mathcal{O}(J_j/J)^2, \tag{43}$$

$$\left.\frac{dM}{\gamma^2 db}\right|_{b_s^* T\to 0} \to \frac{\beta}{4}(a_{1,s} - a_{1,s-1})^2$$

$$= \frac{\beta}{4}[1 + \mathcal{O}(J_j/J)^2], \tag{44}$$

where $s = 1,\ldots,2s_1$ and $c \approx 1.199\,678\,64$ is the solution to $\tanh c = 1/c$. The coefficients $a_{1,s} = s + \mathcal{O}(J_j/J)^2$ and $a_{2,s} = \mathcal{O}(J_j/J)^2$. The easiest way to see this is to first rotate the crystal so the quantization axis is along $\boldsymbol{B}$, as discussed in Appendix B. An expression for $a_{1,s}$ to second order in the J_j/J is given in Appendix B. We note that $b_s^* = \gamma B_{s,s_1}^{\rm lc}(\theta,\phi)$ depends upon s, s_1, and the direction of $\boldsymbol{B}$ when anisotropic interactions are present.

The $C_V(B)$ double peaks are double Schottky anomalies at the reduced induction values $b_s^* \pm \frac{2c}{\beta} + \mathcal{O}(J_j/J)^2$. Hence to $\mathcal{O}(J_j/J)$, the heights and midpoint slopes of the $2s_1$ low-T $M(B)$ steps are uniform and the same as for the isotropic case, but the step positions and hence their plateaus are not. Correspondingly, the heights and relative positions of the $2s_1$ $C_V(B)$ double peaks are uniform and the same as for the isotropic case, but the positions of the zeroes as $T\to 0$ are not. Hence the nonuniversal level-crossing inductions $B_{s,s_1}^{\rm lc}(\theta,\phi)$ fully determine the low-T thermodynamics of weakly anisotropic AFM dimers. This conclusion was obtained previously for Fe_6, Fe_{10}, and Cr_8 rings.[12,14] We remark that this conclusion only holds when level crossing is present, such as when the eigenstates ϵ_s and ϵ_{s-1} have opposite symmetries. In the following, we show that AFM $s_1=1$ dimers with $J_a/J=0.1$ can exhibit level repulsion, which has been observed experimentally in a Ni_2 dimer with $J_a/J = 0.27$,[23] although in neither case did the level repulsion occur between the two lowest energy states. Note that for J_a/J sufficiently large, the $s=0$ and lowest $s=2$ energies repel one another. This lack of level crossing was also noted previously in Mn_9.[58,49]

In the next three sections, we consider the special cases of $s_1 = 1/2$, 1, and 5/2. Then, in Sec. IV and Appendix B, we present our general expression for $B_{s,s_1}^{\rm lc}(\theta,\phi)$ accurate to second order in each of the J_j. We remark that a double peak in the low-T $C_V(B)$ curve has been seen experimentally in a much more complicated Fe_6 ring compound, and was attributed to level crossing.[8]

IV. ANALYTIC RESULTS FOR WEAKLY ANISOTROPIC DIMERS OF ARBITRARY SPIN

A. Induction representation eigenstates first order in the anisotropies

Since the diagonalization of the Hamiltonian matrix is difficult for an arbitrary $\boldsymbol{B}$ combined with an arbitrary combination of spin anisotropy interactions, and must be done separately for each value of s_1, it is useful to consider a perturbation in the relative strengths J_j/J of the anisotropy interactions. We nominally assume $|J_j/J| \ll 1$ for $j = a,c,e,f$. However, to compare with low-T $\boldsymbol{M}(\boldsymbol{B})$ and $C_V(\boldsymbol{B},T)$ experiments at various $\boldsymbol{B}$, one cannot take B to be small. In order to incorporate $\boldsymbol{B}$ accurately, we therefore rotate the crystal axes $(\hat{\boldsymbol{x}},\hat{\boldsymbol{y}},\hat{\boldsymbol{z}})$ to $(\hat{\boldsymbol{x}}',\hat{\boldsymbol{y}}',\hat{\boldsymbol{z}}')$, so that $\boldsymbol{B} = B\hat{\boldsymbol{z}}'$. The rotation matrix, a brief discussion of its ramifications, and the transformed $\tilde{\mathcal{H}}'$ are given in Appendix B.

In these rotated coordinates, the Zeeman interaction $-bS_{z'}$, where $b=\gamma B$, is diagonal. This representation is denoted the induction representation, and has been used in many physical situations, such as in the de Haas–van Alphen effect and in extreme type-II superconductors.[59,60] In the induction representation, we choose the quantum states to be $|\varphi_s^m\rangle$. In the absence of the four anisotropy interactions J_j, $\mathcal{H}' = \mathcal{H}_0'$ is diagonal,

$$\mathcal{H}_0'|\varphi_s^m\rangle = E_s^{m,(0)}|\varphi_s^m\rangle, \tag{45}$$

where

$$E_s^{m,(0)} = -Js(s+1)/2 - mb. \tag{46}$$

The operations of the remaining terms in $\mathcal{H}'$ on the eigenstates $|\varphi_s^m\rangle$ are given in Appendix B. The first-order correc-

tion to the energy in the induction representation, $E^{m,(1)}_{s,s_1} = \langle \varphi^m_s | \mathcal{H}' | \varphi^m_s \rangle$, is found to be

$$E^{m,(1)}_{s,s_1} = -\frac{J_f + 2J_a}{4}[s(s+1)] + \frac{J_a}{2} + \frac{\tilde{J}^{s,s_1}_{f,a}}{2}[m^2 + s(s+1) - 1] + \frac{1}{2}[s(s+1) - 3m^2][\tilde{J}^{s,s_1}_{f,a}\cos^2\theta + \tilde{J}^{s,s_1}_{c,e}\sin^2\theta\cos(2\phi)], \tag{47}$$

where

$$\tilde{J}^{s,s_1}_{f,a} = (1 - \alpha_{s,s_1})\frac{J_f}{2} + \alpha_{s,s_1}J_a, \tag{48}$$

$$\tilde{J}^{s,s_1}_{c,e} = (1 - \alpha_{s,s_1})\frac{J_c}{2} + \alpha_{s,s_1}J_e, \tag{49}$$

and α_{s,s_1} is given by Eq. (29).

Since the θ, ϕ dependence of $E^{m,(1)}_{s,s_1}$ arises from the term proportional to $\tilde{J}^{s,s_1}_{f,a}\cos^2\theta + \tilde{J}^{s,s_1}_{c,e}\sin^2\theta\cos(2\phi)$, it is tempting to think that the thermodynamics with $\tilde{J}^{s,s_1}_{c,e} = 0$ and $\boldsymbol{B} \| \hat{\boldsymbol{z}}$ are equivalent to those with $\tilde{J}^{s,s_1}_{f,a} = 0$ and $\boldsymbol{B} \| \hat{\boldsymbol{x}}$. However, as shown explicitly in the following, the θ, ϕ-independent parts of Eq. (47) strongly break this apparent equivalence, causing the $B^{\rm lc}_{s,s_1}(\theta, \phi)$ for those two cases to differ. This implies that J_f and J_c are experimentally inequivalent, as are J_a and J_e, even to first order in the anisotropy strengths.

B. Level crossings to second order in the anisotropy energies

In Appendix B, we give the details of the evaluation of the second-order energies $E^{m,(2)}_{s,s_1}$. We note that the $E^{m,(2)}_{s,s_1}$ contain divergences at $\gamma B/|J| = 0$, $2s-1$, $2s+3$, $s-1/2$, and $s+3/2$, so that near to those values, one would need to modify the perturbation expansion to take proper account of the degeneracies. Hence the expressions for $E^{m,(2)}_{s,s_1}$ cannot be used in the asymptotic expressions for the thermodynamics. However, as the sth AFM level crossing occurs approximately at $\gamma B/|J| = s$, which is far from any divergences, we can safely use this second-order expansion to obtain an expression for the level crossings to second order in the anisotropy interaction energies. We therefore find an accurate expression for the sth AFM level crossing at the induction $B^{\rm lc}_{s,s_1}$ to second order in the anisotropy interactions for a general s_1 spin dimer by equating $E^{s,(0)}_s + E^{s,(1)}_{s,s_1} + E^{s,(2)}_{s,s_1}$ to $E^{s-1,(0)}_{s-1} + E^{s-1,(1)}_{s-1,s_1} + E^{s-1,(2)}_{s-1,s_1}$, yielding

$$\gamma B^{\rm lc}_{s,s_1} = -Js - \frac{J_f}{4} - \frac{c_{s,s_1}}{2}(2J_a - J_f) - \frac{1}{4}(4s - 3 + 6c_{s,s_1}) \times [J_f\cos^2\theta + J_c\sin^2\theta\cos(2\phi)] + 3c_{s,s_1}[J_a\cos^2\theta + J_e\sin^2\theta\cos(2\phi)] + J\sum_{n=1}^{7} a_n(s,s_1)f_n(\theta,\phi) + \mathcal{O}(\{J_j\})^3, \tag{50}$$

where the first-order coefficients

$$c_{s,s_1} = \frac{[3 + 3s - 5s^2 - 4s^3 + 4s_1(s_1+1)]}{2(2s+1)(2s+3)}, \tag{51}$$

and the second-order coefficients $a_n(s,s_1)$ and angular functions $f_n(\theta,\phi)$ are given in Appendix B. As we shall see, the first-order c_{s,s_1} determines the most interesting behavior of the level-crossing inductions. We note that $\gamma B^{\rm lc}_{s,s_1}$ contains the θ, ϕ-independent terms, $-Js - J_f/4 - c_{s,s_1}(J_a - J_f/2)$, which distinguish J_f from J_c and J_a from J_e.

In particular, we note that the single-ion anisotropy interactions generally behave very differently with increasing step number than do the anisotropic exchange interactions. As shown in detail in the following, for $s_1 = 1/2$, $c_{1,1/2} = 0$, so that the single-ion anisotropy terms are irrelevant. For $s_1 = 1$, $c_{1,1} = \frac{1}{6}$ and $c_{2,1} = -\frac{1}{2}$ have different signs, and for $s_1 = 5/2$, the first three $c_{s,5/2}$ coefficients are $\frac{16}{15}$, $-\frac{4}{35}$, and $-\frac{53}{63}$, respectively, the second being an order of magnitude smaller than the other two, and opposite in sign from the first. This much smaller magnitude of $c_{2,5/2}$ from the other $c_{s,5/2}$ plays a crucial role in identifying the likely presence of significant single-ion anisotropy in $[\mathrm{Fe(salen)Cl}]_2$.

The effects of c_{s,s_1} on the anisotropic exchange interactions is rather different, since both $c_{s,s_1}/2$ and the additional coefficient $(4s - 3 + 6c_{s,s_1})/4$ appear. The latter increases rather monotonically with s. These qualitative differences are verifiable experimentally in careful low-T experiments at high magnetic fields applied at various directions on single crystals of sufficiently large-s_1 dimers for which $|J|$ is sufficiently small.

V. EXACTLY SOLUBLE SPIN-1/2 DIMER

Plots of C_V/k_B and M/γ vs $\gamma B/|J|$ for the isotropic spin-1/2 dimer were given previously.[26] For $s_1 = 1/2$ with an arbitrary $\boldsymbol{B}$ and J_j for $j = a, c, e, f$, the rank-4 Hamiltonian matrix is block diagonal, since $s = 0, 1$ is a good quantum number. The eigenvalues are given by

$$\epsilon_1 = -\frac{J_a}{2} + \frac{J_f}{4}, \tag{52}$$

$$\epsilon_n = -\frac{J_a}{2} + \frac{J_f}{4} - J + \lambda_n, \quad n = 2,3,4, \tag{53}$$

where

$$0 = 4\lambda_n^3 + 4\lambda_n^2 J_f - \lambda_n[J_c^2 - J_f^2 + 4b^2] - 2b^2\sin^2\theta[J_f - J_c\cos(2\phi)]. \tag{54}$$

The cubic equation is easily solved exactly, and the eigenvalues for arbitrary $\boldsymbol{B}$ are given in Appendix A. It is then elementary to write the thermodynamic functions for arbitrary $\boldsymbol{B}$, but the formulas are complicated, so we only present some special cases, for which they simplify greatly.

For the special cases $\boldsymbol{B} \| \hat{\boldsymbol{i}}$ for $i = x, y, z$, the λ^i_n satisfy

$$\lambda^z_n = 0, \quad -\frac{J_f}{2} \pm F_z, \tag{55}$$

$$\lambda_n^{x,y} = -2J_{y,x}, \quad -J_{x,y} \pm F_{x,y}, \tag{56}$$

where

$$F_i = \sqrt{b^2 + J_i^2}, \tag{57}$$

$$J_{x,y,z} = \frac{J_f \pm J_c}{4}, \quad \frac{J_c}{2}, \tag{58}$$

respectively, and where J_x (J_y) corresponds to the upper (lower) sign.

The magnetization for $\boldsymbol{B}||\hat{\boldsymbol{i}}$ is given by

$$M_i = \frac{\gamma b \sinh(\beta F_i)}{F_i \mathcal{D}_i}, \tag{59}$$

$$\mathcal{D}_i = \cosh(\beta F_i) + \Delta_i/2, \tag{60}$$

$$\Delta_x = \exp(-\beta J_x)[\exp(-\beta J) + \exp(2\beta J_y)], \tag{61}$$

$$\Delta_y = \exp(-\beta J_y)[\exp(-\beta J) + \exp(2\beta J_x)], \tag{62}$$

$$\Delta_z = \exp(-\beta J_f/2)[\exp(-\beta J) + 1], \tag{63}$$

respectively. We note that J_a only renormalizes the ground-state energy, and J_e does not appear at all. Hence neither J_a nor J_e affect any measurable quantities for $s_1 = 1/2$. We note that $M_y(J_c) = M_x(-J_c)$ for each B, as expected from $\tilde{\mathcal{H}}_d = -J_c(S_x^2 - S_y^2)/2$.

From Eqs. (52), (53), (55), and (56), the single level crossing induction ($s=1$) for an $s_1 = 1/2$ dimer with $\boldsymbol{B}||\hat{\boldsymbol{i}}$ occurs precisely at

$$\gamma B_{1,1/2}^{\rm lc} = \begin{cases} \sqrt{J^2 + J(J_f \pm J_c)/2}, & \boldsymbol{B}||\hat{\boldsymbol{x}},\hat{\boldsymbol{y}} \\ \sqrt{(J + J_f/2)^2 - J_c^2/4}, & \boldsymbol{B}||\hat{\boldsymbol{z}} \end{cases}, \tag{64}$$

provided that $J + J_{x,y} < 0$ and $J + J_f/2 < 0$, respectively. From our second-order expansion, Eq. (50), $B_{1,1/2}^{\rm lc}(\theta,\phi)$ is found to second order in the J_j to be

$$\gamma B_{1,1/2}^{\rm lc} \approx -J - \frac{J_f}{2} + \frac{(2J + J_f)\sin^2\theta}{8J}[J_f - J_c\cos(2\phi)] + \frac{1}{32J}\{4J_c^2 - 3\sin^4\theta[J_f - J_c\cos(2\phi)]^2\}, \tag{65}$$

where we used $a_1(1,\frac{1}{2}) = \frac{1}{2}$, $a_4(1,\frac{1}{2}) = \frac{1}{8}$, and the other $a_n(1,\frac{1}{2}) = 0$. Plot of examples of $B_{1,1/2}^{\rm lc}(\theta,\phi)$ are given in Fig. 2.

We note that for $\boldsymbol{B}||\hat{\boldsymbol{z}}$, J_f appears to renormalize J to $J' = J + J_f/2$. But, for $\theta \neq 0$, one would require different renormalizations. For instance, our exact Eq. (64) for $\boldsymbol{B}||\hat{\boldsymbol{x}},\hat{\boldsymbol{y}}$ indicates clearly that one would require $J' = J + J_{x,y}$, respectively. Unless special structural circumstances occur that might lead one to suppose a change in the bond lengths in strong magnetic fields,[50] the isotropic Heisenberg interaction J (or J') cannot otherwise depend upon the direction of $\boldsymbol{B}$, especially for $\gamma B \ll |J|$. However, in fits to experiment on $s_1 = 1/2$ dimers, one could treat the effective Heisenberg interaction J' as the weighted midpoint of the level crossing induction, $J' = -\gamma\langle B_{1,1/2}^{\rm lc}(\theta,\phi)\rangle$, where $\langle\cdots\rangle = \int_0^\pi \cdots \sin\theta d\theta \int_0^{2\pi} d\phi/4\pi$. This leads to $J' = J + \frac{1}{3}J_f - \frac{1}{30J}(2J_c^2 + J_f^2) + \mathcal{O}(\{J_j\})^3$. However, from Eq. (50), it evident that for higher spin dimers, $J' \to J'_{s,s_1} = -\gamma\langle B_{s,s_1}^{\rm lc}(\theta,\phi)\rangle/s$ depends upon both s and s_1, complicating the analysis. For simplicity, we choose not to make any such J renormalizations.

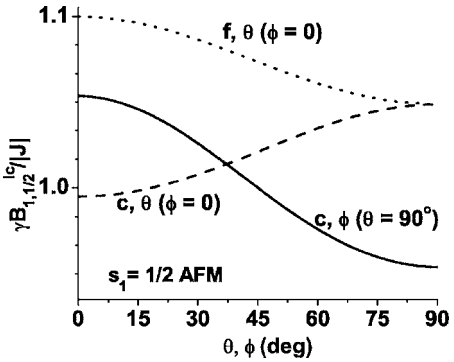

FIG. 2. Plots of $\gamma B_{1,1/2}^{\rm lc}(\theta,0)/|J|$ for the AFM spin-1/2 dimer with $J_c/J = 0.2$, $J_f = 0$ (dashed) and $J_f = 0.2J, J_c = 0$ (dotted), and of $B_{1,1/2}^{\rm lc}(\pi/2,\phi)/\gamma|J|$ for $J_c/J = 0.2$, $J_f = 0$ (solid).

As an example of the effect of anisotropic exchange interactions upon the magnetization of $s_1 = 1/2$ dimers, in Fig. 3, we plotted the low-T M/γ vs $\gamma B/|J|$ with $J_c = 0.2J$, $J_f = 0$ for $\boldsymbol{B}||\hat{\boldsymbol{z}}$ (solid) and $\boldsymbol{B}||\hat{\boldsymbol{x}}$ (dashed), along with the isotropic case $J_c = J_f = 0$ (dotted). Although for $\boldsymbol{B}||\hat{\boldsymbol{z}}$, B at the step is slightly reduced from its isotropic interaction value, for $\boldsymbol{B}||\hat{\boldsymbol{x}}$, the magnetization step occurs at a larger B. These results are consistent with Eq. (64). The midpoint slopes are universal, in accordance with Eq. (44). In addition, the shape of the step appears also to be universal.

The specific heat of an $s_1 = 1/2$ dimer with $\boldsymbol{B}||\hat{\boldsymbol{i}}$ is

$$C_{Vi} = \frac{k_B\beta^2\mathcal{N}_i}{\mathcal{D}_i^2}, \tag{66}$$

where the $\mathcal{D}_i$ are given by Eq. (60), and the $\mathcal{N}_i$ are given in Appendix A. Plots at low T of C_V/k_B vs $\gamma B/|J|$ for $s_1 = 1/2$

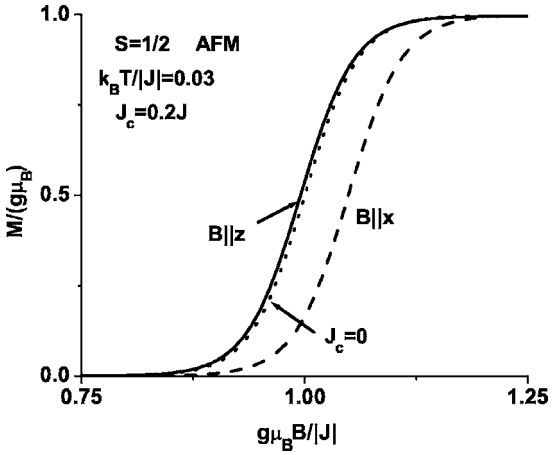

FIG. 3. Plots of M/γ vs $\gamma B/|J|$ at $k_BT/|J| = 0.03$ for the AFM spin-1/2 dimer with $J_c = 0.2J$, $J_f = 0$, with $\boldsymbol{B}||\hat{\boldsymbol{z}}$ (solid), $\boldsymbol{B}||\hat{\boldsymbol{x}}$ (dashed), along with the isotropic case $J_c = J_f = 0$ (dotted).

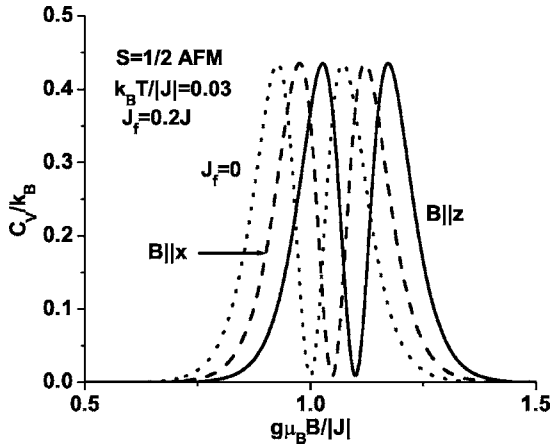

FIG. 4. Plot of C_V/k_B vs $\gamma B/|J|$ for the AFM spin-1/2 dimer with $J_f=0.2J$, $J_c=0$ at $k_BT/|J|=0.03$ with the same curve notation as in Fig. 2.

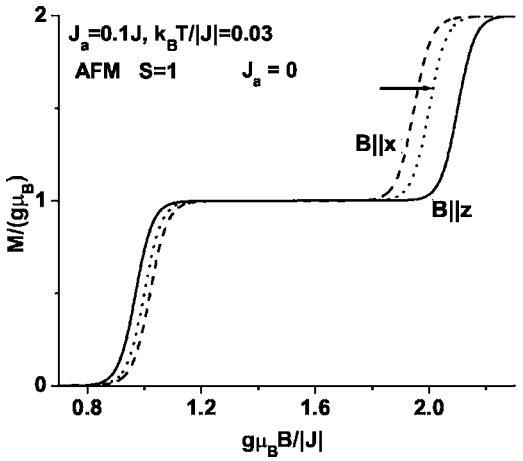

FIG. 5. Plot at $k_BT/|J|=0.03$ and $J_a/J=0.1$ of M/γ vs $\gamma B/|J|$ for the AFM spin-1 dimer. The curve notation is the same as in Fig. 2, except that the isotropic case (dotted) curve is for $J_a=0$.

dimers with the corresponding axial anisotropic exchange energy $J_f=0.2J$ with $J_c=0$ are shown in Fig. 4. We note the universal curve shapes, but nonuniversal level crossing positions, in quantitative agreement with Eqs. (40)–(42). In Fig. 4, the position of the central minimum in C_V tracks that of the midpoint of the magnetization step with the same parameters.

VI. ANALYTIC AND NUMERICAL RESULTS FOR $s_1=1$ AND 5/2

A. Spinor dimer

For dimers with $s_1=1$, the allowed s values are $s=0,1,2$. Since the even and odd dimer s states cannot mix, the three $s=1$ states are decoupled from the six remaining $s=0,2$ states. They satisfy a cubic equation given in Appendix A. For $\boldsymbol{B}||\hat{\boldsymbol{i}}$ with $i=x,y,z$, this cubic equation simplifies to a linear and a quadratic equation, as for the $s=1$ eigenstates of $s_1=1/2$ dimers.

The remaining six eigenstates corresponding nominally to $s=0,2$ are in general all mixed. The matrix leading to the hexatic equation from which the six eigenvalues can be obtained is given in Appendix A. That is sufficient to evaluate the eigenvalues for $s_1=1$ using symbolic manipulation software. When combined with the three $s=1$ eigenvalues, one can then use Eqs. (34) and (35) to obtain the resulting exact magnetization and specific heat at an arbitrary $\boldsymbol{B}$. The combined nine eigenvalues depend upon all four anisotropy parameters J_j for $j=a,c,e,f$.

To the extent that the eigenvalues can be obtained from the solutions to either linear or quadratic equations, the expressions for the $B_{s,1}^{\rm lc}$ along a crystal axis direction are simple, and are given in Appendix A. In the anisotropic exchange case $J_a=J_e=0$, the first level crossing induction $B_{1,1}^{\rm lc}$ with $\boldsymbol{B}||\hat{\boldsymbol{i}}$ is identical to $B_{1,1/2}^{\rm lc}$, the level crossing with $s_1=1/2$ given by Eq. (64). The two level crossing inductions for $s_1=1$ can be found to first order in the anisotropy energies by evaluating Eq. (50) for $s_1=1$ and $s=1,2$.

The first-order coefficients in $B_{s,1}^{\rm lc}$ are $c_{1,1}=\frac{1}{6}$ and $c_{2,1}=-\frac{1}{2}$. From these simple first-order results, it is possible to understand the qualitatively different behavior obtained with local, single-ion, anisotropy from that obtained with anisotropic exchange. In the isotropic case $J_j=0\,\forall\, j$, the first and second level crossings occur at $-J$ and $-2J$, respectively. For each induction direction, the signs of the contributions of the anisotropic exchange interactions J_c and J_f to $B_{2,1}^{\rm lc(1)}+2J$ and $B_{1,1}^{\rm lc(1)}+J$ are the same, whereas the signs of the contributions of the single-ion interaction energies J_a and J_e to $B_{2,1}^{\rm lc(1)}+2J$ and $B_{1,1}^{\rm lc(1)}+J$ are the *opposite*.

To illustrate this point, in Fig. 5 we plotted the low-T $M(B)$ for the axial single-ion anisotropy $J_a/J=0.1$. We note that for $\boldsymbol{B}||\hat{\boldsymbol{x}}$, the first level crossing occurs at an induction higher than with $J_a=0$, but the second level crossing appears at a lesser induction than for the isotropic case.

The second-order coefficients in $B_{s,1}^{\rm lc}$ are easily found to be $a_1(1,1)=\frac{1}{2}$, $a_2(1,1)=-1=a_3(1,1)$, $a_4(1,1)=\frac{1}{8}$, $a_5(1,1)=-\frac{1}{4}$, $a_6(1,1)=-\frac{11}{40}$, $a_7(1,1)=-\frac{2}{27}$, $a_1(2,1)=\frac{17}{4}$, $a_2(2,1)=\frac{7}{2}$, $a_3(2,1)=\frac{1}{4}$, $a_4(2,1)=a_6(2,1)=\frac{5}{16}$, $a_5(2,1)=\frac{3}{8}$,and $a_7(2,1)=0$. Using these values, we can generate plots of $B_{s,1}^{\rm lc}(\theta,\phi)$ accurate to second order in all of the anisotropy parameters.

To illustrate the different effects of the four anisotropy interactions, in Fig. 6, we plotted $\gamma B_{s,1}^{\rm lc}(\theta,0)/|J|$ for both $s_1=1$ level crossings $s=1,2$ for the four cases in which one of the $J_j/J=0.1$ and the other $J_j=0$. As can be seen from Fig. 6, the $s=2$ step exhibits remarkable symmetry. The two anisotropic exchange interactions J_c and J_f have opposite θ-dependent deviations from their joint value approximately at $\theta=90°$. The two single-ion interactions J_a and J_e have that value as their average, and also display opposite θ dependencies. However, the $s=1$ step is somewhat different. The J_a and J_e curves also have opposite θ-dependent deviations from their average value, but the signs of the deviations are opposite to those in the $s=2$ curves, and the magnitudes of their θ variations are considerably smaller. However, the signs of the θ variations of the J_c and J_f $s=1$ curves are the same as for the $s=2$ curves. Hence if one of the four anisotropy interactions is dominant, by measuring $B_{s,1}^{\rm lc}(\theta,\phi)$ for

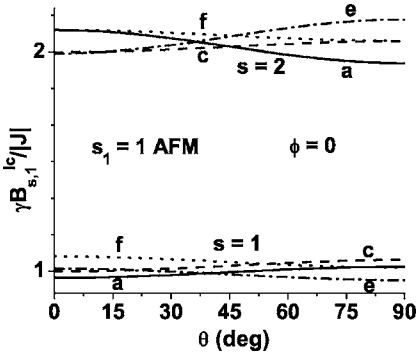

FIG. 6. Plots of the level crossing inductions $\gamma B_{s,1}^{\mathrm{lc}}(\theta,0)/|J|$ for $s_1=1$ AFM dimers, with $J_a/J=0.1$ (solid), $J_c/J=0.1$ (dashed), $J_e/J=0.1$ (dash-dotted), and $J_f/J=0.1$ (dotted). The curves are correspondingly labeled a, c, e, f.

$s=1,2$, one can fully determine the dominant anisotropy parameter.

In Fig. 7, we plotted the azimuthal dependence of the level-crossing inductions, $\gamma B_{s,1}^{\mathrm{lc}}(\pi/2,\phi)/|J|$ for the two cases $J_c/J=0.1$ and $J_e/J=0.1$, with the other anisotropy parameters absent. Note that the axial anisotropy parameters J_a and J_f by themselves do not lead to any ϕ dependencies. As seen in Fig. 7, both J_c curves decrease with increasing ϕ, whereas the J_e curve increases for $s=1$, but decreases for $s=2$, and the effect at $s=2$ is larger than for the J_c curve. Thus a measurement of the ϕ dependence of $B_{s,1}^{\mathrm{lc}}$ can distinguish the presence of J_c from J_e anisotropy. Thus the two independent measurements of $B_{s,1}^{\mathrm{lc}}(\theta,0)$ and $B_{s,1}^{\mathrm{lc}}(\pi/2,\phi)$ are probably sufficient to completely determine the values of the four anisotropy parameters, even if all four are present and of similar magnitude.

In short, the case $s_1=1$ is sufficient to exhibit the very different behaviors obtained from the single-ion, local spin anisotropy interactions from those obtained from the anisotropic exchange interactions. As s_1 increases beyond 1, the situation becomes not only more complicated, but also more interesting, as shown in the following.

B. Spin-5/2 dimer

For $s_1=5/2$, one of the cases of greatest experimental interest, when $\tilde{\mathcal{H}}_a$ and $\tilde{\mathcal{H}}_e$ are present, none of the allowed

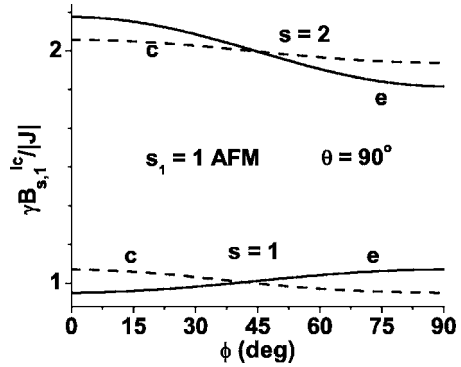

FIG. 7. Plot of the $s=1,2$ level crossing inductions $\gamma B_{s,1}^{\mathrm{lc}}(\pi/2,\phi)/|J|$ for $s_1=1$ AFM dimers, with $J_e/J=0.1$ (solid), $J_c/J=0.1$ (dashed). The curves are correspondingly labeled e, c.

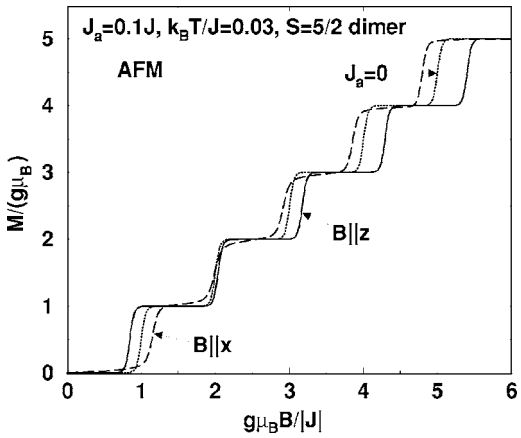

FIG. 8. Plot at $k_BT/|J|=0.03$ and $J_a/J=0.1$ of M/γ vs $\gamma B/|J|$ for the AFM spin-5/2 dimer. The curve notation is the same as in Fig. 3.

s,m values is a true quantum number. That is, $\tilde{\mathcal{H}}_a$ and $\tilde{\mathcal{H}}_e$ cause all of the states with nominally odd or even s to mix with one another. For $\boldsymbol{B}||\hat{\boldsymbol{i}}$ for $i=x,y,z$, this simplifies in the crystal representation, as for $s_1=1$, since only states with odd or even m values in the appropriately chosen representation can mix. By using symbolic manipulation software, it is possible to solve for the exact eigenvalues of the $s_1=5/2$ dimer. However, because the analytic expressions for the eigenvalues are much more complicated than those for $s_1=1$ presented in Appendix A, we shall not attempt to present them, but will instead focus upon their numerical evaluation for specific cases.

In Figs. 8 and 9, we plot M/γ vs $\gamma B/|J|$ for the two low-T cases of AFM $s_1=5/2$ dimers, $J_a=0.1J$, and $J_c=0.1J$, respectively, with the other $J_j=0$, taking $k_BT/|J|=0.03$. Each of these curves exhibits the universal step behavior predicted in Eqs. (43) and (44). Corresponding C_V/k_B vs $\gamma B/|J|$ curves also exhibit the universal double peak behaviors predicted in Eqs. (40)–(42), and are shown elsewhere.[61]

In Fig. 8 for $J_a/J=0.1$, we note that the $s=2$ step is nearly isotropic, as there is much less angular variation than for any

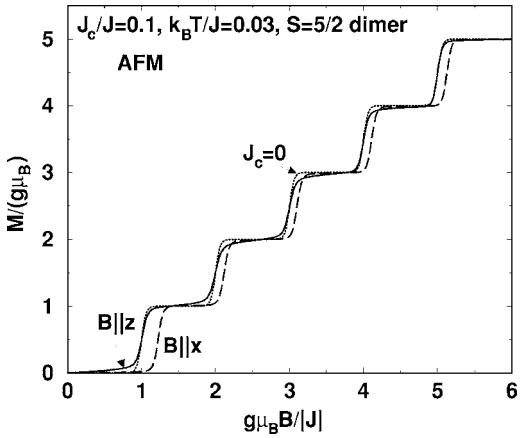

FIG. 9. Plot at $k_BT/|J|=0.03$ and $J_c/J=0.1$ of M/γ vs $\gamma B/|J|$ for the AFM spin-5/2 dimer. The curve notation is the same as in Fig. 3.

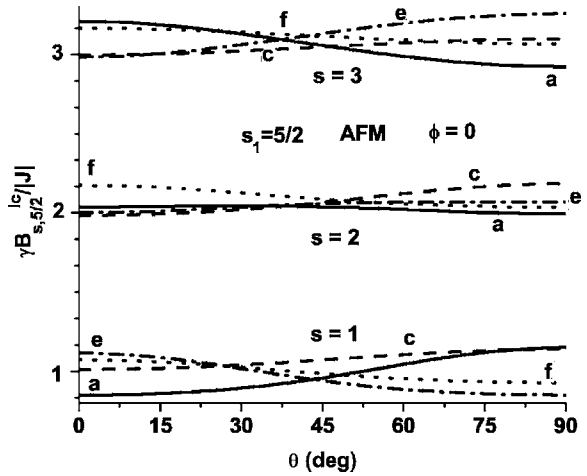

FIG. 10. Plot of the lowest $s=1,2,3$ level crossing inductions $\gamma B^{\rm lc}_{s,5/2}(\theta,0)/|J|$ vs θ at $\phi=0$ for $s_1=5/2$ AFM dimers, with $J_a/J=0.1$ (solid), $J_c/J=0.1$ (dashed), $J_e/J=0.1$ (dash-dotted), and $J_f/J=0.1$ (dotted). The curves are correspondingly labeled a, c, e, f.

of the other steps. This is because the change in sign in the deviations of the level crossing inductions from $-sJ$ occurs very close to the $s=2$ step, as predicted by the first-order coefficient $c_{s,5/2}$. We reiterate that $c_{1,5/2}=\frac{16}{15}$, $c_{2,5/2}=-\frac{4}{35}$, and $c_{3,5/2}=-\frac{53}{63}$, so that the sign change occurs just before the $s=2$ step, making $|c_{2,5/2}|\ll 1$, accounting quantitatively for this effect.

In Fig. 9 for $J_c/J=0.1$, the step behavior is very different than for $J_a/J=0.1$ pictured in Fig. 8. There are no changes in sign in the deviations of the level crossing inductions from $-sJ$. For $\boldsymbol{B}||\hat{z}$, there is little difference from the isotropic case. However, for $\boldsymbol{B}||\hat{x}$, all five level crossings occur at inductions higher than for the isotropic case, but their deviation from $-sJ$ is nonmonotonic, with a minimum deviation (and hence the minimum anisotropy of the level crossing inductions) occurring at the third crossing.

In Figs. 10 and 11, $\gamma B^{\rm lc}_{s,5/2}(\theta,0)/|J|$ and $\gamma B^{\rm lc}_{s,5/2}(\pi/2,\phi)/|J|$ corresponding to Figs. 6 and 7 are plotted. For clarity, we only show the lowest three level crossing inductions. Figure 10 shows that the sign change in the behaviors of the single ion J_a and J_e occurs closer to the second level crossing than for $s_1=1$. Note that the J_a curve for $B^{\rm lc}_{2,5/2}(\theta,0)$ is nearly symmetric about $\theta=45^\circ$, suggesting a near vanishing of the first-order contribution, and the slight bulge centered at that midpoint is due to the second-order contributions. As in Fig. 7, there are no sign changes for the anisotropic exchange interactions J_c and J_f. Furthermore, it is evident from this figure that $B^{\rm lc}_{2,5/2}(\theta,0)$ is nearly constant for the two single-ion interactions J_a and J_e, consistent with Fig. 8.

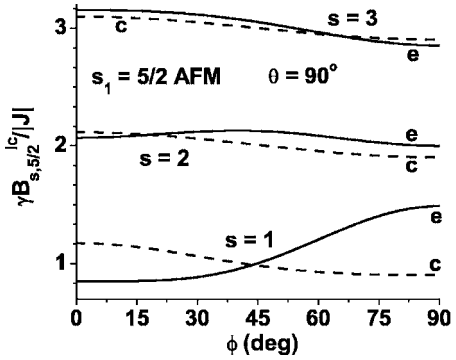

FIG. 11. Plot of the lowest $s=1,2,3$ level crossing inductions $\gamma B^{\rm lc}_{s,5/2}(\pi/2,\phi)/|J|$ vs ϕ at $\theta=\pi/2$ for $s_1=5/2$ AFM dimers, with $J_e/J=0.1$ (solid), $J_c/J=0.1$ (dashed). The curves are correspondingly labeled e, c.

Further support for this notion is seen in Fig. 11, in which $\gamma B^{\rm lc}_{s,5/2}(\pi/2,\phi)/|J|$ is plotted for $J_c/J=0.1$ and $J_e/J=0.1$. Clearly, for $s=2$, the main ϕ dependence of the J_e curve arises from the second-order effects proportional to $\cos^2(2\phi)$. By contrast, the first-order term $\propto\cos(2\phi)$ leads to a pronounced $B^{\rm lc}_{1,5/2}(\pi/2,\phi)$ variation for $J_e/J=0.1$. Note also that the sign of the ϕ variation in the third level crossing for $J_e/J=0.1$ is opposite to that of the first crossing, and is nearly absent in the second crossing, so that the sign change of both the θ and ϕ deviations from the isotropic level crossing behavior is a first-order effect for J_e. By contrast, J_c shows no sign changes in either the θ or the ϕ dependencies in these figures.

We remark that this greatly reduced anisotropy of the second level crossing for the two single-ion interactions is strong evidence for the presence of one or both of them in $[\mathrm{Fe(salen)Cl}]_2$, as discussed in more detail in Sec. IX.

Our results for $B^{\rm lc}_{s,7/2}(\theta,0)$ and $B^{\rm lc}_{s,7/2}(\pi/2,\phi)$ with $s_1=7/2$ are not shown for brevity. We only remark that the second-order effects are stronger than for $s_1=5/2$, and that for $J_e/J=0.1$, $B^{\rm lc}_{1,7/2}(\pi/2,\phi)$ has such a strong ϕ dependence that the first and second level crossings are approximately equal at $\phi=90^\circ$, making the first two level crossings difficult to distinguish.

VII. HARTREE APPROXIMATION

A. First-order thermodynamics

In the self-consistent Hartree approximation, originally developed in the early days of atomic physics, the exchange interactions are neglected, and the direct (in this case, anisotropy) interactions are treated self-consistently to first order.[62] In magnetism, this later sometimes came to be known as the strong exchange limit.[17,18,30,46,53] In this approximation, s and m are still good quantum numbers, so the partition function

$$Z^{(1)}=\sum_{s=0}^{2s_1}\sum_{m=-s}^{s}e^{-\beta E^m_{s,s_1}}, \tag{67}$$

where $E^m_{s,s_1}=E^{m,(0)}_s+E^{m,(1)}_{s,s_1}$. Although it is difficult to perform the summation over the m values analytically, it is, nevertheless, elementary to evaluate Z numerically for an arbitrary B, θ, ϕ, and T from the eigenstate energies. The magnetization in the Hartree approximation is

$$M^{(1)}(B,\theta,\phi)=\frac{\gamma}{Z^{(1)}}\sum_{s=0}^{2s_1}\sum_{m=-s}^{s}me^{-\beta E^m_{s,s_1}}. \tag{68}$$

Similarly, the specific heat in the Hartree approximation is

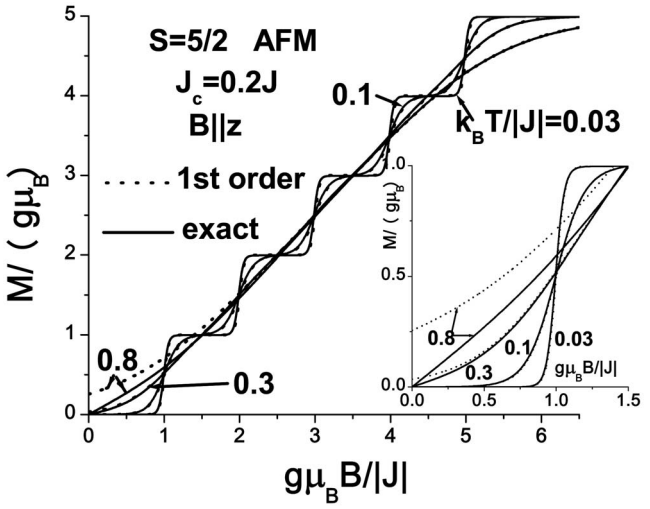

FIG. 12. Comparison of M/γ vs $\gamma B/|J|$ obtained using the Hartree asymptotic form (dotted) with the exact calculation (solid), for the $s_1=5/2$ AFM dimer with $J_c=0.2J$, $J_a=J_e=J_f=0$, at $k_BT/|J|=0.03$, 0.1, 0.3, 0.8, as indicated. Inset: expanded view of the region $0\leq\gamma B/|J|\leq 1.5$.

$$C_V^{(1)}(B,\theta,\phi)\approx\frac{k_B\beta^2}{(Z^{(1)})^2}\left[Z^{(1)}\sum_{s=0}^{2s_1}\sum_{m=-s}^{s}(E_{s,s_1}^m)^2e^{-\beta E_{s,s_1}^m}-\left(\sum_{s=0}^{2s_1}\sum_{m=-s}^{s}E_{s,s_1}^m e^{-\beta E_{s,s_1}^m}\right)^2\right]. \tag{69}$$

As a test of the accuracy of this Hartree calculation, we have compared the Hartree and exact $M(B)$ obtained for the $s_1=5/2$ dimer with $J_c=0.2J$ and $\boldsymbol{B}\|\hat{z}$ at various T values in Fig. 12. The corresponding comparison between the Hartree and exact $C_V(B)$ is shown in Fig. 13. We see that the curves evaluated using the Hartree and the exact expressions for M and C_V with $s_1=5/2$ are indistinguishable at $k_BT/|J|=0.03$. The C_V curves are noticeably different at $k_BT/|J|=0.1$ for $\gamma B/|J|<0.4$, and at $k_BT/|J|=0.3$ they are noticeably different for $\gamma B/|J|<2.6$. Corresponding noticeable differences in the M curves at the same B values appear at T values roughly three times as high as in the C_V curves.

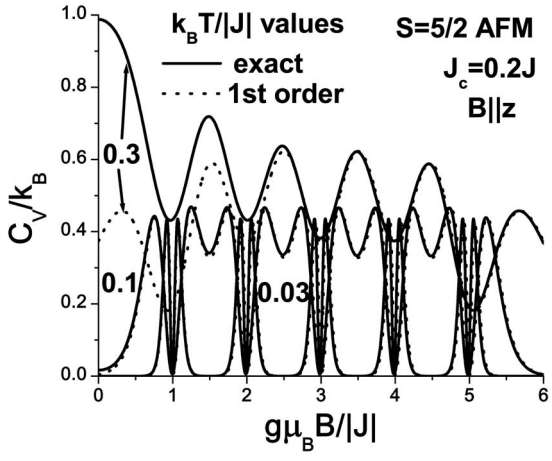

FIG. 13. Comparison of C_V/k_B vs $\gamma B/|J|$ obtained using the Hartree asymptotic form (dotted) with the exact calculation (solid), for the $s_1=5/2$ AFM dimer with $J_c=0.2J$, $J_a=J_e=J_f=0$, at $k_BT/|J|=0.03$, 0.1, 0.3, as indicated.

At very low T, $k_BT/|J|\ll 1$, the most important states in this perturbative scheme are the minima for each s value, E_{s,s_1}^s, which determine the level crossings in the Hartree approximation. As $T\to 0$, we can ignore all of the $m\neq s$ states in Eqs. (67)–(69). This two-level approximation is the basis for the universal behavior given by Eqs. (40)–(44), which fits all of the exact curves we presented reasonably well.

B. First-order response functions

1. Inelastic neutron-scattering cross section

Two response functions relevant for the study of SMM's are the INS cross section $S(\boldsymbol{B},\boldsymbol{q},\omega)$ and the EPR susceptibility $\chi(\boldsymbol{B},\omega)$ in strong magnetic inductions $\boldsymbol{B}$. We first consider the low-T inelastic neutron cross section $S(\boldsymbol{B},\boldsymbol{q},\omega)$ taking $\hat{\boldsymbol{d}}=\hat{z}$ as pictured in Fig. 1. It is customary to write the operators in the crystal representation.[26,59] With INS, one can also probe the dimer with a strong magnetic field at various directions with respect to both the dimer axis and the scattering plane. To the extent that the eigenstates $\{|\phi_n\rangle\}$ and their energies ϵ_n can be evaluated exactly,

$$S(\boldsymbol{B},\boldsymbol{q},\omega)=\sum_{\alpha,\beta=1}^{3}(\delta_{\alpha,\beta}-\hat{q}_\alpha\hat{q}_\beta)\sum_{n,n'=1}^{n_{s_1}}e^{-\beta\epsilon_n}\delta(\omega+\epsilon_n-\epsilon_{n'})\times\langle\phi_n|\tilde{S}_\alpha(\boldsymbol{q},0)|\phi_{n'}\rangle\langle\phi_{n'}|\tilde{S}_\beta^\dagger(\boldsymbol{q},0)|\phi_n\rangle, \tag{70}$$

where $\tilde{S}_\alpha(\boldsymbol{q},0)=US_\alpha(\boldsymbol{q},0)U^\dagger$, $S_\alpha(\boldsymbol{q},0)=S_{1,\alpha}e^{i\boldsymbol{q}\cdot\boldsymbol{d}}+S_{2,\alpha}e^{-i\boldsymbol{q}\cdot\boldsymbol{d}}$, and U is the unitary operator that diagonalizes $\mathcal{H}$.[20,26] When exact expressions for $S(\boldsymbol{B},\boldsymbol{q},\omega)$ are tedious to obtain, it is straightforward to obtain it in the Hartree approximation, $S^{(1)}(\boldsymbol{B},\boldsymbol{q},\omega)$. But to do so, it is easiest to define the axes in the induction representation, for which $\{|\phi_n\rangle\}=\{|\tilde{\varphi}_s^m\rangle\}$ and the $\hat{\boldsymbol{e}}_\alpha=\hat{\boldsymbol{x}}',\hat{\boldsymbol{y}}',\hat{\boldsymbol{z}}'$ for $\alpha=1$, 2, 3, respectively. In the Hartree approximation obtained by setting the $|\tilde{\varphi}_s^m\rangle=|\varphi_s^m\rangle$, the bare wave functions, $S^{(1)}(\boldsymbol{B},\boldsymbol{q},\omega)$ for an arbitrary B,θ,ϕ is then

$$\begin{aligned}S_1^{(1)}=\sum_{s=0}^{2s_1}\sum_{m=-s}^{s}e^{-\beta E_{s,s_1}^m}\Big(&\cos^2(\boldsymbol{q}\cdot\boldsymbol{d})\sin^2\theta_{b,q}\mathcal{F}_{1,s_1}^{m,s(0)}(\omega,\theta,\phi)\\&+\sin^2(\boldsymbol{q}\cdot\boldsymbol{d})\sin^2\theta_{b,q}\mathcal{F}_{2,s_1}^{m,s(0)}(\omega,\theta,\phi)\\&+\cos^2(\boldsymbol{q}\cdot\boldsymbol{d})\frac{2-\sin^2\theta_{b,q}}{4}\mathcal{F}_{3,s_1}^{m,s(0)}(\omega,\theta,\phi)\\&+\sin^2(\boldsymbol{q}\cdot\boldsymbol{d})\frac{2-\sin^2\theta_{b,q}}{4}\mathcal{F}_{4,s_1}^{m,s(0)}(\omega,\theta,\phi)\Big),\end{aligned} \tag{71}$$

where $\boldsymbol{q}\cdot\boldsymbol{d}=qd\cos\theta_q$ is invariant under the rotation, $2\boldsymbol{d}$ is the vector separating the dimer spins, $\theta_{b,q}$ is the angle between $\boldsymbol{q}$ and $\boldsymbol{B}$, and

$$\mathcal{F}_{1,s_1}^{m,s(0)}=m^2\delta(\omega), \tag{72}$$

$$\mathcal{F}^{n,s(0)}_{2,s_1} = \sum_{\sigma'=\pm 1} \delta(\omega + E^m_{s,s_1} - E^m_{s+\sigma',s_1})(D^m_{s+(\sigma'+1)/2,s_1})^2, \tag{73}$$

$$\mathcal{F}^{m,s(0)}_{3,s_1} = \sum_{\sigma=\pm 1} \delta(\omega + E^m_{s,s_1} - E^{m+\sigma}_{s,s_1})(A^{\sigma m}_s)^2, \tag{74}$$

$$\mathcal{F}^{m,s(0)}_{4,s_1} = \sum_{\sigma,\sigma'=\pm 1} \delta(\omega + E^m_{s,s_1} - E^{m+\sigma}_{s+\sigma',s_1})(C^{-(\sigma'+1)/2-\sigma\sigma' m}_{s+(\sigma'+1)/2,s_1})^2, \tag{75}$$

where the coefficients are given, respectively, by Eqs. (21), (1), and (20), and we have suppressed the ω, θ, ϕ arguments of the $\mathcal{F}^{m,s(i)}_{n,s_1}$ functions for simplicity of presentation. In Eq. (71), the only dependencies upon the anisotropy energies is in the first-order eigenstate energies $E^m_{s,s_1} = E^{m,(0)}_s + E^{m,(1)}_{s,s_1}$ given by Eqs. (46) and (47), respectively. The $\boldsymbol{B}=0$ limit is easily obtained by setting $B=\theta=0$ and $\theta_{b,q}=\theta_q$.

Corrections to the wave functions first order in the anisotropy interactions lead to additional transitions with strengths first and second order in the anisotropy energies.[63] Studying the weak transitions $(s,m)\rightarrow(s',m')$ with $s'=s$, $m\pm 1$, ± 2, ± 3 and $s'=s\pm 1$, $m'=m\pm 2$ can provide further direct measurements of the anisotropic exchange interactions J_c and J_f.

2. Electron paramagnetic resonance susceptibility

In an EPR experiment, one applies a strong magnetic field, plus a weak oscillatory transverse field, leading to the overall induction $\boldsymbol{B}=B\hat{\boldsymbol{z}}'+B_\perp[\hat{\boldsymbol{x}}'\cos(\omega t)-\sigma\hat{\boldsymbol{y}}'\sin(\omega t)]$, where we assume the oscillatory induction precesses clockwise (counterclockwise) for $\sigma=\pm 1$.[59,64–66] For a weak transverse induction $B_\perp$, one measures the resulting linear response $\chi_{-\sigma,\sigma}(\boldsymbol{B},\omega)$, which is written in terms of the total spin raising and lowering operators $S_\pm$ defined in the induction representation,[59,64] the transformed Hamiltonian of which is described in Appendix B. In principle, an exact expression for $\chi_{-\sigma,\sigma}(\boldsymbol{B},\omega)$ can be obtained by starting in the induction representation with the basis $\{|\varphi^m_s\rangle\}$, diagonalizing $\mathcal{H}$ with the unitary operator V, $V\mathcal{H}V^\dagger=\tilde{H}'$, and the new basis $\{|\tilde{\phi}_n\rangle\}$ is obtained from $|\tilde{\phi}_n\rangle=V|\varphi^m_s\rangle$, leading to $\tilde{\mathcal{H}}'|\tilde{\phi}_n\rangle=\tilde{\epsilon}_n|\tilde{\phi}_n\rangle$. One then has

$$\chi_{-\sigma,\sigma}(\boldsymbol{B},\omega) = \frac{\gamma^2}{\pi Z}\sum_{n,n'=1}^{n_{s_1}} e^{-\beta\tilde{\epsilon}_n}\langle\tilde{\phi}_n|\tilde{S}_{-\sigma}(0)|\tilde{\phi}_{n'}\rangle\langle\tilde{\phi}_{n'}|\tilde{S}_\sigma(0)|\tilde{\phi}_n\rangle \times\left(\frac{1}{\omega+\tilde{\epsilon}_n-\tilde{\epsilon}_{n'}+i\eta}-\frac{1}{\omega-\tilde{\epsilon}_n+\tilde{\epsilon}_{n'}+i\eta}\right), \tag{76}$$

where $\tilde{S}_\sigma(0)=VS_\sigma(0)V^\dagger$. It is then elementary to obtain $\chi''_{-\sigma,\sigma}(\omega)$ in the Hartree approximation valid to first order in the anisotropy parameters, which is well-behaved for all induction values. The imaginary part of $\chi_{-\sigma,\sigma}$ is then

$$\chi^{(1)''}_{-\sigma,\sigma}(\boldsymbol{B},\omega) = \frac{\gamma^2}{Z^{(1)}}\sum_{s=0}^{2s_1}\sum_{m=-s}^{s} e^{-\beta E^m_{s,s_1}}[s(s+1)-m^2-\sigma m] \times[\delta(E^m_{s,s_1}-E^{m+\sigma}_{s,s_1}+\omega)-\delta(E^{m+\sigma}_{s,s_1}-E^m_{s,s_1}+\omega)], \tag{77}$$

where $E^m_{s,s_1}=E^{m,(0)}_s+E^{m,(1)}_{s,s_1}$ is given by Eqs. (46) and (47) and $Z^{(1)}$ is given by Eq. (67). The arguments of the δ function give rise to the resonant frequencies first order in the anisotropy energies, or to the first-order resonant magnetic inductions,

$$\gamma B^{(1)}_{\rm res} = \pm\omega + \frac{(2m+\sigma)}{2} g_{s,s_1}(\theta,\phi), \tag{78}$$

$$g_{s,s_1}(\theta,\phi) = \tilde{J}^{s,s_1}_{f,a}(1-3\cos^2\theta) - 3\tilde{J}^{s,s_1}_{c,e}\sin^2\theta\cos(2\phi), \tag{79}$$

where $\tilde{J}^{s,s_1}_{f,a}$ and $\tilde{J}^{s,s_1}_{c,e}$ are given by Eqs. (48) and (49), respectively, and we have ignored the processes that give rise to finite transition widths.[67] By varying the direction and magnitude of $\boldsymbol{B}$, it is possible to obtain sufficient information to fit all of the parameters in the model. At low T the $m=s$ states dominate, so that only $\sigma=-1$ is allowed. By increasing $\boldsymbol{B}$ past the sth level crossing, one can probe the effective sth state of the AFM dimer using EPR.

We have extended these results to include the corrections to the wave functions first order in the anisotropy interactions.[63] With these corrections, additional EPR transitions are present, which can provide additional information useful in experimental identification of the anisotropy interactions. It is shown that there are ten additional resonant magnetic induction strengths of the forms

$$\gamma B^{(1)}_{\rm res} = \pm a_n\omega + b_n g_{s,s_1}(\theta,\phi) + c_n h_{s,s_1}(\theta,\phi), \tag{80}$$

$$h_{s,s_1}(\theta,\phi) = -(J+J_f/2+J_a) + \tilde{J}^{s,s_1}_{f,a}(1+\cos^2\theta) + \tilde{J}^{s,s_1}_{c,e}\sin^2\theta\cos(2\phi), \tag{81}$$

where the a_n, b_n, and c_n are listed in Appendix B. We note that these additional resonant inductions are first order in the anisotropy interactions, but have amplitudes that are second order in the anisotropy interactions, so that in most cases, they may be difficult to detect, but their detection in certain materials would provide a clear signal of the presence of significantly strong anisotropy interactions. In addition, resonant inductions with $c_n\neq 0$ are generally very large.

To illustrate one example of an effect of local spin anisotropy upon the EPR transitions, we consider the simple case of an $s_1=1$ AFM dimer with the only nonvanishing anisotropy energy $J_a/J=0.1$ and $\theta=\pi/4$. The energy levels for this system are pictured in Fig. 14. In Fig. 15, the EPR transition energies vs $\gamma B/|J|$ for the $s_1=1$ AFM dimer with $J_a/J=0.1$ and $\theta=\pi/4$ are shown. The widths of the lines are proportional to the strengths of the EPR matrix elements. Note that the ground state at $B=0$ is approximately $|\psi^0_0\rangle$, but its energy is slightly negative due to an admixture of this

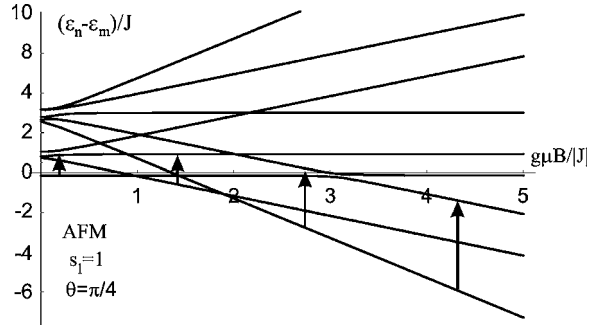

FIG. 14. Plot of the exact eigenvalues $\epsilon_n/|J|$ vs $\gamma B/|J|$ for $s_1=1$ AFM dimers with $J_a/J=0.1$ and $\theta=\pi/4$. The arrows represent the strongest EPR transitions at their corresponding field strengths.

state with the nominal $|\psi_2^m\rangle$ states with even m, as shown in Appendix A. The EPR matrix elements are very small at these B values, as the transitions only exist due to the admixture of the wave functions. At higher B strengths, the ground state goes through two level crossings, with the first level crossing being to the lowest energy $s=1$ state, which is nominally $|\psi_1^1\rangle$, with some mixture of the other $|\psi_1^m\rangle$ states. The leading transition is to the nominal $|\psi_1^0\rangle$ state. Then, the second level crossing causes the ground state to be the nominal $|\psi_2^2\rangle$ state, which is of course modified by the mixing with the nominal $|\psi_0^0\rangle$ and the other nominal $|\psi_2^m\rangle$ for $m=0,-2$. Note that near to $\gamma B/|J|=3$, there is a level repulsion. The leading EPR transition is to the nominal $|\psi_2^1\rangle$ state, and because of the strong matrix elements, the splitting of the energies due to the level repulsion should be observable in EPR experiments. We note that recent EPR experiments on the Ni_2 dimer, $Na_2Ni_2(C_2O_4)_3(H_2O)_2$, appear consistent with these predictions, with the experimental anisotropy $J_a/J=0.27$.[23]

VIII. AFM DIMERS WITH STRONG ANISOTROPY INTERACTIONS

Finally, we consider some cases of strong anisotropy interactions, in which one or more of the J_j is comparable to J in magnitude. The cases of interest are those for which the anisotropy interactions can remove the level crossing effects in AFM dimers that give rise to the $2s_1+1$ $M(B)$ steps and $C_V(B)$ double peaks. These cases generally occur for strong FM anisotropy interactions, but there are some examples in which they can occur with strong AFM anisotropy interactions. We first consider the case of $s_1=1/2$ dimers, for which the situation can be analyzed analytically, at least for $\boldsymbol{B}||\hat{\boldsymbol{i}}$. Then, we consider the $s_1=5/2$ case numerically.

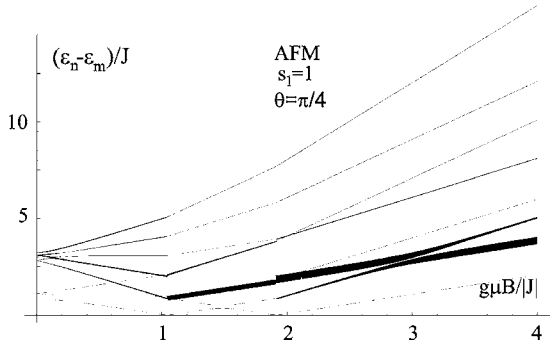

FIG. 15. Plot of the EPR transition energies $(\epsilon_n-\epsilon_1)/|J|$ vs $\gamma B/|J|$ from the ground state for the $s_1=1$ AFM dimer with $J_a/J=0.1$ and $\theta=\pi/4$. The widths of the lines are proportional to the strengths of the matrix elements for the transitions.

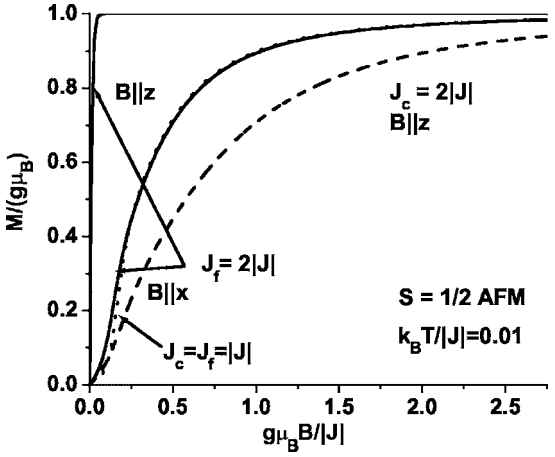

FIG. 16. Plots of M/γ vs $\gamma B/|J|$ at $k_BT/|J|=0.01$ with $J_f=2|J|$ (solid) for both $\boldsymbol{B}||\hat{\boldsymbol{x}},\hat{\boldsymbol{z}}$, $J_c=J_f=|J|$ (dotted), and $J_c=2|J|$ with $\boldsymbol{B}||\hat{\boldsymbol{z}}$ (dashed) for the $s_1=1/2$ AFM dimer.

A. Analytic and numerical results for $s_1=1/2$ dimers

For the $s_1=1/2$ dimer, the energies for $\boldsymbol{B}||\hat{\boldsymbol{i}}$ are given by Eqs. (52)–(58). We are interested in examining the cases in which the anisotropy is strong enough to cause the level crossing to disappear. Strong anisotropy with J_c and J_f having the same sign as J do not differ significantly from the weak-coupling cases, as they do not remove the level crossing, and do not affect significantly the heights of the magnetization step and the number and shapes of the $C_V(B)$ double peaks, but just shift their positions, as for weak anisotropy. There are then three AFM ($J<0$) cases of interest. These are (i) $J_c=J_f=|J|$, (ii) $J_f=2|J|$, and (iii) $J_c=2|J|$. The $M(B)$ and $C_V(B)$ curves for these cases with $\boldsymbol{B}||\hat{\boldsymbol{z}}$ at the very low-T value $k_BT/|J|=0.01$ are shown as the solid, dotted, and dashed curves in Figs. 16 and 17, respectively.

For case (i), $J_c=J_f=|J|$, the same four eigenvalues are obtained for $\boldsymbol{B}||\hat{\boldsymbol{z}}$ and $\boldsymbol{B}||\hat{\boldsymbol{x}}$. Assuming $J<0$, these are ranked from highest to lowest as

$$\epsilon_{4,1}=-J/2\pm\sqrt{b^2+J^2/4}, \tag{82}$$

$$\epsilon_3=-J, \tag{83}$$

$$\epsilon_2=0. \tag{84}$$

Note that $\epsilon_1=\epsilon_2$ only at $b=0$ (where $\epsilon_3=\epsilon_4$), ϵ_1 decreases with increasing b, and ϵ_4 increases with increasing b, so the levels get further apart with increasing b. In this case, $M(B)$ shown as the dotted curve in Fig. 16 is broad, even at the

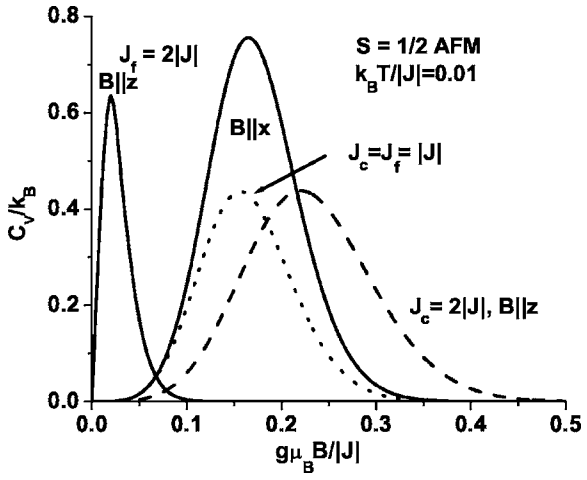

FIG. 17. Plots of C_V/k_B vs $\gamma B/|J|$ at $k_BT/|J|=0.01$ with $J_f=2|J|$ (solid) for both $\boldsymbol{B}||\hat{x},\hat{z}$, $J_c=J_f=|J|$ (dotted), and $J_c=2|J|$ with $\boldsymbol{B}||\hat{z}$ (dashed) for the $s_1=1/2$ AFM dimer.

very low T value plotted. In addition, $C_V(B)$, shown as the dotted curve in Fig. 17, exhibits a single Schottky-like anomaly, but with a different shape than that of the standard Schottky case, which arises from a splitting of the two lowest energies linear in b at $b=0$. In this case, the peak value of C_V/k_B is 0.439 229, the same as the uniform double peak value, but the peak position is at $b=\sqrt{2c|J|/\beta}$, where $c=1.199\ 678\ 64$.

Next, we examine case (ii), $J_f=2|J|$, $J_c=0$. In this case the energies are different for the two field directions. For $\boldsymbol{B}||\hat{z}$,

$$\epsilon_4 = -J, \tag{85}$$

$$\epsilon_{3,1} = \pm b, \tag{86}$$

$$\epsilon_2 = 0. \tag{87}$$

At $b=0$, these energies comprise a triply degenerate (or spin-1) ground state at 0 and an excited $+|J|$ state. With increasing b, ϵ_1 decreases linearly, and ϵ_4 increases linearly, crossing ϵ_4 at $b=|J|$, which does not affect the low-T thermodynamics. In this case, $M(B)$ is a sharp step at $B=0$, shown as a solid curve in Fig. 16, and $C_V(B)$ is a conventional spin-1 Schottky anomaly at low b, as shown by the left solid curve in Fig. 17. From Eqs. (86) and (87), C_V/k_b has a maximum value at 0.637 203 at $b=1.880\ 677\ 5/\beta$. Note that the larger maximum value than in the other $C_V(B)$ cases arises from the higher degeneracy as $b\to 0$.

For $\boldsymbol{B}||\hat{x}$, the energies for case (ii) are

$$\epsilon_{4,1} = -J/2 \pm \sqrt{b^2 + J^2/4}, \tag{88}$$

$$\epsilon_{2,3} = 0. \tag{89}$$

At $b=0$, the ground state is again triply degenerate with energy 0, and the excited state has energy $|J|$. With increasing b, ϵ_1 separates from ϵ_2 and ϵ_3, curving below them, and ϵ_4 increases quadratically. For this induction direction there is no level crossing, but there is some $\boldsymbol{b}$ anisotropy at finite T, because of the quadratic vs linear b dependencies. C_V/k_B has the maximum value 0.761 802 at $b=\sqrt{2c_1|J|/\beta}$, where $c_1=2.654\ 658$, which is noticeably different from the case with $\boldsymbol{B}||\hat{z}$. The $M(B)$ and $C_V(B)$curves are the right solid curves in Figs. 16 and 17, respectively.

Now we consider case (iii), $J_c=-2J$, $J_f=0$. Again, there are slight differences for $\boldsymbol{B}||\hat{z}$ and $\boldsymbol{B}||\hat{x}$. For $\boldsymbol{B}||\hat{z}$, the eigenstate energies are

$$\epsilon_{4,1} = -J \pm \sqrt{b^2 + J^2}, \tag{90}$$

$$\epsilon_3 = -J, \tag{91}$$

$$\epsilon_2 = 0. \tag{92}$$

At $b=0$, the ground state is doubly degenerate at energy 0. The other two states have energies $|J|$ and $2|J|$, respectively. As b increases, ϵ_1 decreases below ϵ_2, and ϵ_4 increases monotonically. Hence there is no level crossing, but at low T, two levels are relevant, in a fashion slightly different from a standard Schottky specific heat anomaly. The low-T $M(B)$ and $C_V(B)$ curves for this induction direction are shown as the dashed curves in Figs. 16 and 17, respectively. We note that they are rather similar from those of case (i), but have the broadest $M(B)$ increase and $C_V(B)$ peak of the three cases considered. C_V/k_B has the peak value 0.439 229 which is the same as the uniform double-peak value, but its position is at $b=2\sqrt{c|J|/\beta}$, where $c=0.199\ 678\ 64$.

For $\boldsymbol{B}||\hat{x}$, we have

$$\epsilon_4 = -2J, \tag{93}$$

$$\epsilon_{3,1} = -J/2 \pm \sqrt{b^2 + J^2/4}, \tag{94}$$

$$\epsilon_2 = 0. \tag{95}$$

At $b=0$, the eigenstates are the same as for the field in the z direction, with a doubly degenerate ground state at 0, and excited states at $|J|$ and $2|J|$. However, the field dependence is a bit different than for the z direction. Again the ground state decreases with increasing b, but the energy scale of the curvature is $|J|/2$ instead of $|J|$. In addition, ϵ_3 can cross ϵ_4 at $b=\sqrt{2}|J|$. This level crossing is irrelevant to the low-T behavior, however, but modifies the $M(B)$ curve somewhat at finite T.

B. AFM $s_1=5/2$ dimers with strong anisotropy interactions

We now consider some cases of strong anisotropy interactions in the $s_1=5/2$ dimer. In Fig. 18, we present low-T plots of $M(B)$ with $J_c=J_f=c|J|$, where $c=0.2$, 0.4, 0.6, 0.8, 0.9, and 1, as indicated. For the weak-coupling case $c=0.2$, the steps have uniform height. With increasing c, the curves shift monotonically to lower b values. Slight deviations in the uniformity of the step height are detectable in the first two steps for $c=0.4$, but the nonuniformity in the step height is progressively more pronounced for $c=0.6$ and 0.8, respectively. However, for $c=0.9$, the individual steps have completely disappeared, and are replaced by what appears to be a single, broad step centered at $b/J\approx 0.5$. At $c=1$, $M(B)$ rises to its maximum value with a very steep slope at $b=0$, not

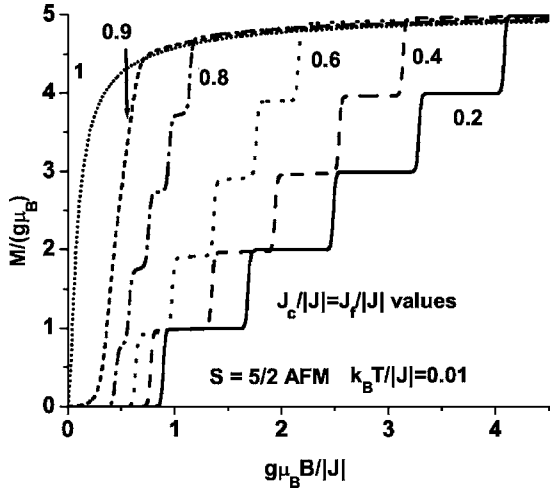

FIG. 18. Plots of M/γ vs $\gamma B/|J|$ at $k_BT/|J|=0.01$ with $J_c=J_f=c|J|$ for the AFM $s_1=5/2$ dimer. The cases $c=0.2$ (solid), $c=0.4$ (dashed), $c=0.6$ (dotted), $c=0.8$ (dot-dashed), $c=0.9$ (short dashed), and $c=1$ (short dotted) are shown.

showing any evidence for any level crossings.

Next, we investigated the effects of large J_a. In Fig. 19 we plotted M/γ vs $\gamma B/|J|$ for $J_a=c|J|$, with $c=0.1$ (solid), 0.2 (dashed), 0.3 (dotted), 0.4 (dot-dashed), 0.5 (short dashed), and 0.6 (short dotted). We see the effects of strong J_a are very different from those of strong J_c and J_f shown in Fig. 18. Instead of the step positions decreasing monotonically with increasing $J_c=J_f$, as J_a increases, the highest three step positions decrease with increasing J_a, but the lowest two step positions increase with increasing J_a.

We now consider the case of large J_c. In Fig. 20, we plotted M/γ vs $b/|J|$ at $k_BT/|J|=0.01$ for the $s_1=5/2$ AFM dimer with $J_c=c|J|$, where $c=0.1$, 0.2, 0.3, 0.4, and 0.5. These results are shown respectively as the solid, dashed, dotted, dot-dashed, and short dotted curves. Unlike the strong anisotropic exchange case pictured in Fig. 18 and the strong axial single-ion anisotropy case pictured in Fig. 19,

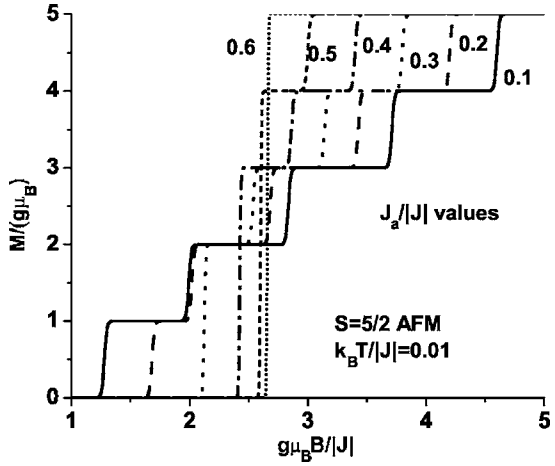

FIG. 19. Plots of M/γ vs $\gamma B/|J|$ at $k_BT/|J|=0.01$ with $J_a=c|J|$ for the AFM $s_1=5/2$ dimer. The cases $c=0.1$ (solid), $c=0.2$ (dashed), $c=0.3$ (dotted), $c=0.4$ (dot-dashed), $c=0.5$ (short dashed), and $c=0.6$ (short dotted) are shown.

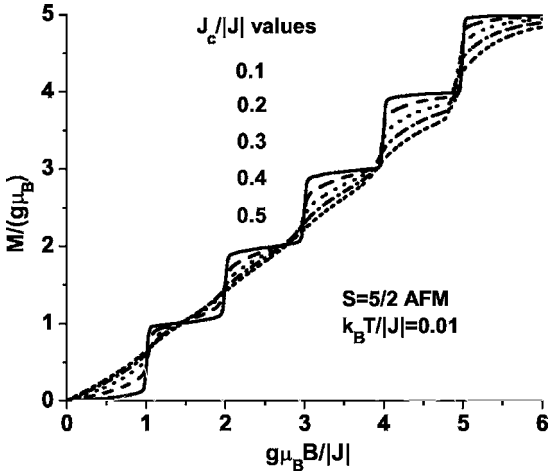

FIG. 20. Plots of M/γ vs $\gamma B/|J|$ at $k_BT/|J|=0.01$ with $J_c=c|J|$ for the AFM $s_1=5/2$ dimer. The cases $c=0.1$ (solid), $c=0.2$ (dashed), $c=0.3$ (dotted), $c=0.4$ (dot-dashed), and $c=0.5$ (short dotted) are shown.

these curves do not shift significantly to lower b values with increasing $J_c/|J|$, but the step shapes are greatly altered. With $c=0.4$, the first two steps are hard to discern, but rounded remnants of the three last steps are evident. At $c=0.5$, the third step is hard to detect, and the remnants of the last two steps are reduced in magnitude. We remark that the curve with $c=-0.3$ is indistinguishable from the dotted curve for $c=0.3$, so that in this case, strong J_c/J of either sign can grossly alter the $M(\boldsymbol{B})$ step behavior.

In Fig. 21, we show C_V/k_B vs $b/|J|$ low-T curves for some of the AFM $s_1=5/2$ cases pictured in Figs. 18–20. The solid and dot-dashed curves on the left-hand side of the figure correspond to $J_c=J_f=c|J|$ with $c=0.9$ and 1, respectively, the solid and dot-dashed curves in the central portion of the figure correspond to $J_a/|J|=0.4$ and 0.5, respectively, and the dashed curve running throughout the domain pictured corresponds to $J_c=0.5|J|$. We note that for the combined exchange anisotropy case shown, strong anisotropy pushes the

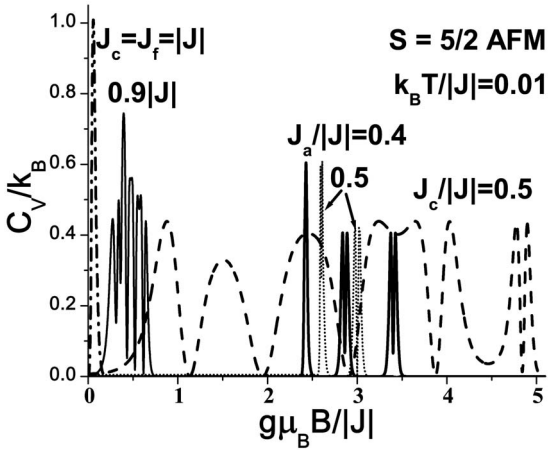

FIG. 21. Plots of C_V/k_B vs $\gamma B/|J|$ at $k_BT/|J|=0.01$ for the AFM $s_1=5/2$ dimer. The cases $J_c=J_f=c|J|$ for $c=0.9$ (solid) and $c=1$ (dot-dashed), $J_a=c|J|$ for $c=0.4$ (solid) and 0.5 (short-dashed) and $J_c=0.5|J|$ (thick dashed) are shown.

$C_V(B)$ peaks to lower b, and squeezes them together, so that they tend to overlap. At the limiting case $J_c=J_f=|J|$, the individual level crossings have been eliminated, and all ten of the peaks are combined into a single Schottky anomaly. For the local axial anisotropy interaction, strong FM anisotropic interactions squeeze the $C_V(B)$ together in the middle of the domain, with the limiting case of a single peak at $J_a/|J|=0.6$. For the strong azimuthal anisotropic exchange interaction case, however, strong FM anisotropy shifts the double peak positions only slightly, and broadens the double peaks, so that only the highest set is clearly discernable, even at the very low-T value plotted. In each case, the deviation of the peak height from the two-level prediction, Eq. (41), is substantial, indicating more than two levels are important at low T, as for the three-level system with $s_1=1/2$ and $J_f=2|J|$. Thus the different types of strong spin anisotropy lead to clearly different low-T $C_V(B)$ behaviors for $s_1>1/2$ dimers.

IX. SUMMARY AND CONCLUSIONS

In summary, we solved for the low-temperature magnetization and specific heat of equal spin s_1 antiferromagnetic dimer single molecule magnets with S_2, C_{2h}, or C_{2v} molecular group symmetry, including the most general set of anisotropic spin exchange and single-ion anisotropy interactions quadratic in the spin operators. The magnetization and specific heat exhibit steps and zeroes, respectively, at the nonuniversal level crossing induction values $B^{\rm lc}_{s,s_1}(\theta,\phi)$, but the magnetization steps and their midpoint slopes, plus the two peaks surrounding the specific heat zeroes all exhibit universal behavior at sufficiently low temperatures to first order in the anisotropy interaction strengths. For weak anisotropy, we showed that the essential s,s_1 dependencies of $B^{\rm lc}_{s,s_1}(\theta,\phi)$ are given by the single first-order function c_{s,s_1} in Eq. (51). The most direct measurement of the level crossing $B^{\rm lc}_{s,s_1}(\theta,\phi)$ is obtained by the low-T steps in the magnetization of single crystals. Strong anisotropy interactions generally lead to highly nonuniversal behavior in antiferromagnetic dimers. Single-ion anisotropy interactions lead to much richer variations of $B^{\rm lc}_{s,s_1}(\theta,\phi)$ than do those obtained from anisotropic exchange interactions, provided that $s_1>1/2$. These differences are especially prominent for $s_1=5/2$.

For the most general quadratic anisotropic spin interactions at an arbitrary $\boldsymbol{B}$, we derived simple, asymptotic analytic expressions for the low-temperature magnetization, specific heat, inelastic neutron-scattering cross section, and electron paramagnetic response susceptibility, which are accurate for weak anisotropy. We also derived an accurate expression for the level crossing induction $B^{\rm lc}_{s,s_1}(\theta,\phi)$, enabling fast and accurate fits to experimental data.

There were two low-T $M(B)$ studies of Fe_2 dimers.[28,29] For μ-oxalatotetrakis(acetylacetonato) Fe_2, all five peaks in dM/dH were measured in pulsed magnetic fields H. These evenly spaced peaks were entirely consistent with just the isotropic Heisenberg interaction, and indicated little, if any, spin anisotropy and biquadratic effects.[28]

On the other hand, studies of the first two to three dM/dH peaks in powdered samples of $[Fe(salen)Cl]_2$, where salen is N,N'-ethylenebis(salicylideneiminato), were much more interesting.[29] These data showed a broad first peak at $B=17-20$ T that was only partially resolvable into two separate peaks, followed by a sharp second peak at $B=36$ T. These data are consistent with axial and/or azimuthal single-ion anisotropy of strength $|(J_a+J_e)/J|\approx 0.1$, as obtained from the derivatives of the curves shown in Fig. 8, and a powder sampling of Eq. (50) and the data shown in Figs. 10 and 11. These figures also apply for the S_2 symmetry by letting $\hat{z}\rightarrow\hat{z}_1$, etc., as described in detail in Appendix A. Usually, $|J_e/J_a|<1$, but to determine the precise values of each, one would require single-crystal data in various $\boldsymbol{B}$ directions.

However, the existing data on $[Fe(salen)Cl]_2$ appear to be inconsistent with a predominant anisotropic exchange interactions of either J_c or J_f types. It is also inconsistent with an isotropic, biquadratic Heisenberg interaction of the form $-J^*(\boldsymbol{S}_1\cdot\boldsymbol{S}_2)^2$, which would add $-J^*s^3$ to $B^{\rm lc}_{s,s_1}(\theta,\phi)$ in Eq. (50). A biquadratic exchange changes the spacings between the level crossings, but does not change either the angular dependencies of the level crossings in single crystals or the widths of the powder-sampled level crossings, inconsistent with the experiments.[29] In comparing the two materials cited above, it appears that the interaction of a Cl^- ion neighboring each Fe^{3+} ion leads to strong single-ion anisotropy effects. In order to verify this hypothesis and to elucidate the details of the interactions, further experiments using single crystals in different field orientations on this and related Fe_2 dimers with one to three similarly bonded Cl^- ions are urged.[31,32]

We note also that strong evidence for very strong $(J_a/J=0.27)$ axial single-ion anisotropy was presented in the Ni_2 dimer, $Na_2Ni_2(C_2O_4)_3(H_2O)_2$,[23] but it appears that azimuthal single-ion anisotropy was not included in the analysis. On the other hand, from the two zero-field splittings of the low-lying triplet states observed in INS studies of the two spin-1 Ni chain compounds, $Ni(C_5D_{14}N_2)_2$-$N_3(PF_6)$ (NDMAP) and $Ni(C_9H_{24}N_4)(NO_2)ClO_4$ (NTENP), it appears that both J_a and a smaller J_e were present.[40,41] From Eq. (A14) in Appendix A, those gaps could also contain contributions from J_f and J_c, respectively. However, in INS studies, the detailed form factors were employed to rule out such anisotropic exchange interactions.[40,41] The measured zero-field gaps of the triplet state relative to the singlet ground state were 0.42, 0.52, and 1.89 meV in NDMAP with $J=-2.8$ meV,[42] and 1.06(1), 1.15(1), and 1.96(1) meV in NTENP, respectively, and $J=-4.67$ meV.[41] In their model, they assumed only an axial single-ion anisotropy, which they found to be $J_a/J=0.25$. Assuming the zero-field gaps correspond to $|J|+2|J_a|$, $|J|+|J_a|+|J_e|$, and $|J|+|J_a|-|J_e|$, relative to the ground state, as for $s_1=1$ dimers in Appendix A, we obtain for NTENP, $J_a=-0.85$ meV, and $|J_e|=0.04$ meV, so that $J_a/J=0.18$, a bit less than in the Ni_2 dimer above,[23] but we also have $|J_e/J|=0.01$. For NDMAP, we obtain $J_a=-1.42$ meV, and $|J_e|=0.05$ meV, corresponding to $J_a/J=0.51$ and $J_e/J=0.02$. We note that a model with only axial single-ion anisotropy fit the specific-heat data with $J_a/J=0.3$, where they used $J=-2.58$ meV,[43] but the zero-field INS gap splittings are much more direct measurements of J_a,J_e. Hence Ni_2, which has very strong single-ion anisotropy, has axial single-ion anisotropy intermediate between

that in the two AFM Ni chain compounds, NDMAP and NTENP. We suggest that Ni_2 may also have a weak azimuthal single-ion anisotropy, as directly observed in NDMAP and NTENP.[40,41]

In addition, three well-defined steps in the Cr_2 AFM dimer, $Cs_3Cr_2Cl_9$, were found,[25] but such steps were smeared in the AFM Cr_2 $s_1=3/2$ dimer studied by INS, $Cs_3Cr_2Br_9$, due to field-induced magnetic ordering.[24] In addition, the zero-field splitting was fit to a weak axial single-ion anisotropy with $J_a=-0.01$ meV, and with $J=-1.03$ meV, $J_a/J=0.01$. An important question for the future is whether any azimuthal single-ion interaction J_e might also be present in that compound.[24,68] This is because $Cs_3Cr_2Br_9$ is thought to have an AFM spin-flop state, for which a small J_e would break the axial symmetry responsible for the Goldstone mode, opening a gap in the spin fluctuation spectrum, as possibly observed in INS studies.[24,68] Hence it is crucial to have as many possibilities for identifying any such possible presence of even a small amount of J_e. In order to aid in the analysis of future data on this and other systems, we will publish separately additional details relevant for further INS and EPR studies to elucidate this question.[63]

We also urge single-crystal data on the high-spin $s_1=7/2$ Gd_2 AFM dimer, $[Gd(AmPh)]_2\cdot 2CHCl_3$, where AmPh is (tris((2-hydroxybenzyl)amino)ethyl)amine.[33,34] From preliminary fits to experiment, $J=-0.0056$ meV,[33] which is sufficiently small that all seven level crossings ought to be observable at sufficiently low T. We note that for $s_1=7/2$, the lowest three first-order coefficients are $c_{s,7/2}=2$, $\frac{2}{7}$, $-\frac{13}{21}$, respectively, so the θ,ϕ dependencies of the single-ion contributions to the first level crossing are very large, and the sign change occurs slightly above the second level crossing. Second-order effects will also be large. We would also like to see single-crystal magnetization studies of $s_1=1/2$ dimers lacking in predicted single-ion anisotropy effects, to determine the relative strength of any anisotropic exchange interactions J_c and/or J_f.[19,21,22,26] To aid in the fits, we derived simple, useful formulas for the magnetization and specific heat at low temperature and sufficiently large magnetic induction. More important, we derived accurate analytic formulas for the electron paramagnetic resonance susceptibility $\chi(\boldsymbol{B},\omega)$ and the inelastic neutron scattering $S(\boldsymbol{B},\boldsymbol{q},\omega)$, which allow for a precise determination of the various microscopic anisotropy energies.

With either single-ion anisotropy or anisotropic exchange interactions, the total spin s is not a good quantum number, unless $s_1=1/2$, potentially modifying our understanding of quantum tunneling processes in single molecule magnets. Extensions of this work to SMM's with higher numbers of magnetic ions might also be possible to fit a variety of experimental results using a smaller, consistent set of model parameters than has generally been employed.[6,55] We emphasize that the study of antiferromagnetic equal-spin dimer single molecule magnets, for which the most general set of quadratic single-ion anisotropy and anisotropic exchange interactions are so simple that they can be studied analytically, may be an important, and perhaps even the best, tool for attaining a more fundamental understanding of the underlying physics of more general single molecule magnets.

ACKNOWLEDGMENTS

We thank the Max-Planck-Institut für Physik komplexer Systeme, Dresden, Germany, the University of North Dakota, Grand Forks, ND, USA, and Talat S. Rahman for their kind hospitality and support. We also thank N. S. Dalal, B. Grenier, and S. Stolbov for useful discussions. This work was supported by the Netherlands Foundation for the Fundamental Research of Matter and by the NSF under Contract No. NER-0304665.

APPENDIX A

1. General dimer Hamiltonians

In general, the single-ion and exchange Hamiltonians for a dimer may be written as[46,53]

$$\mathcal{H}=\sum_{i=1}^{2}\boldsymbol{S}_i\cdot\overleftrightarrow{\boldsymbol{D}}_{i,i}\cdot\boldsymbol{S}_i+\boldsymbol{S}_1\cdot\overleftrightarrow{\boldsymbol{D}}_{1,2}\cdot\boldsymbol{S}_2. \tag{A1}$$

Here we only treat symmetric matrices $\boldsymbol{D}_{i,i'}$. For $g=D_{2h}$, each of these matrices are diagonal in the same basis, which we take to be the molecular $(\hat{\boldsymbol{x}},\hat{\boldsymbol{y}},\hat{\boldsymbol{z}})$ coordinate basis. For lower symmetries, however, the principle axes of each of the three matrices are generally different. As discussed in textbooks,[69] each symmetric matrix can be diagonalized using three rotations, by $\phi_{i,i'}$ about the z axis, followed by a rotation by $\theta_{i,i'}$ about the rotated x axis, and then by $\psi_{i,i'}$ about the rotated $\tilde{z}$ axis. This leads to the principle axes $\hat{\tilde{\boldsymbol{x}}}_{i,i'}$, $\hat{\tilde{\boldsymbol{y}}}_{i,i'}$, and $\hat{\tilde{\boldsymbol{z}}}_{i,i'}$. After these three diagonalizations, the Hamiltonian may be written as $\mathcal{H}=\mathcal{H}_{ex}+\mathcal{H}_{si}$, where

$$\mathcal{H}_{ex}=-J\boldsymbol{S}_1\cdot\boldsymbol{S}_2-J_f(\boldsymbol{S}_1\cdot\hat{\tilde{\boldsymbol{z}}}_{12})(\boldsymbol{S}_2\cdot\hat{\tilde{\boldsymbol{z}}}_{12})-J_c[(\boldsymbol{S}_1\cdot\hat{\tilde{\boldsymbol{x}}}_{12})(\boldsymbol{S}_2\cdot\hat{\tilde{\boldsymbol{x}}}_{12})-(\boldsymbol{S}_1\cdot\hat{\tilde{\boldsymbol{y}}}_{12})(\boldsymbol{S}_2\cdot\hat{\tilde{\boldsymbol{y}}}_{12})], \tag{A2}$$

$$\mathcal{H}_{si}=-\sum_{i=1}^{2}\{J_i\boldsymbol{S}_i^2+J_{a,i}(\boldsymbol{S}_i\cdot\hat{\tilde{\boldsymbol{z}}}_i)^2+J_{e,i}[(\boldsymbol{S}_i\cdot\hat{\tilde{\boldsymbol{x}}}_i)^2-(\boldsymbol{S}_i\cdot\hat{\tilde{\boldsymbol{y}}}_i)^2]\}, \tag{A3}$$

where we have set the single-ion local axis vectors $\hat{\tilde{\boldsymbol{x}}}_i\equiv\hat{\tilde{\boldsymbol{x}}}_{i,i}$, etc., and the constants are given by linear combinations of the diagonalized matrix elements $\overleftrightarrow{\tilde{\boldsymbol{D}}}_{i,i'}$.[46] For equal-spin dimers with S_2, C_{2v}, or D_{2h} symmetry, $J_{a,1}=J_{a,2}=J_a$ and $J_{e,1}=J_{e,2}=J_e$.

Now, for D_{2h} symmetry, this reduces exactly to the Heisenberg interaction, $\mathcal{H}_a+\mathcal{H}_e+\mathcal{H}_f+\mathcal{H}_c$, given in Eqs. (3)–(6), plus a constant. For C_{2v} symmetry, the anisotropic exchange parts are also given by Eqs. (5) and (6). However, for $g=C_{2v}$, since $D_{11,yz}=-D_{22,yz}\neq 0$, the single-ion matrices are not diagonal in the same representation as is the anisotropic exchange matrix. For $g=S_2$, all of the elements of $\overleftrightarrow{\boldsymbol{D}}_{nn}\neq 0$. In these cases, we rotate the coordinates to the direction of $\hat{z}_\mu=\hat{\tilde{z}}_1$. This overall rotation is first a rotation about the z axis by $\phi_{1,1}$ followed by a rotation about the rotated x axis by $\theta_{1,1}$. It leaves only the transformation angle $\mu=\psi_{1,1}$

to describe the rotated azimuthal vectors $\hat{\boldsymbol{x}}_\mu$ and $\hat{\boldsymbol{y}}_\mu$. For the S_2 symmetry, a similar rotation is required for the anisotropic exchange interactions, which is analogously parametrized by $\tilde{\mu}=\psi_{1,2}$. We then have

$$\mathcal{H}_{si}^{g}=-\sum_{i=1}^{2}[J_a S_{i,z_\mu}^2+J_e\cos(2\mu)(S_{i,x_\mu}^2-S_{i,y_\mu}^2)+c_i^g J_e\sin(2\mu)\times\{S_{i,x_\mu},S_{i,y_\mu}\}], \tag{A4}$$

$$\mathcal{H}_{ae}^{S_2}=-J_f S_{1,z_{\tilde{\mu}}}S_{2,z_{\tilde{\mu}}}-J_c\cos(2\tilde{\mu})(S_{1,x_{\tilde{\mu}}}S_{2,x_{\tilde{\mu}}}-S_{1,y_{\tilde{\mu}}}S_{2,y_{\tilde{\mu}}})-J_c\sin(2\tilde{\mu})(S_{1,x_{\tilde{\mu}}}S_{2,y_{\tilde{\mu}}}+S_{1,y_{\tilde{\mu}}}S_{2,x_{\tilde{\mu}}}), \tag{A5}$$

where $c_i^{S_2}=1$ and $c_i^{C_{2v}}=(-1)^{i+1}$.

Now, we first transform back to the molecular representation, and then transform to the induction representation. As a result of the overall process, S_2 symmetry can be incorporated into the J_e term of the eigenstate energies by letting $\theta\rightarrow\theta-\theta_{1,1}$ and $\phi\rightarrow\phi-\phi_{1,1}-\psi_{1,1}-\pi/2$, and the J_c term can similarly be incorporated into the eigenstates by letting $\phi\rightarrow\phi-\phi_{1,2}-\psi_{1,2}-\pi/2$. For the C_{2v} symmetry, the induction representation can be obtained for the J_e term by letting $\phi\rightarrow\phi+(-1)^i\mu$, where i is the site number. That is, spins 1 and 2 have different effects. For the S_2 symmetry, all results arising from single-ion anisotropy can be obtained from the D_{2h} results by shifting $\theta\rightarrow\theta-\theta_{1,1}$ and $\phi\rightarrow\phi-\phi_{1,1}-\psi_{1,1}-\pi/2$, and all results for the anisotropic exchange interactions can be obtained from the D_{2h} results by replacing $\theta\rightarrow\theta-\theta_{1,2}$ and $\phi\rightarrow\phi-\phi_{1,2}-\psi_{1,2}-\pi/2$. For the C_{2v} symmetry, the anisotropic exchange results are identical to those of D_{2h} symmetry, but the single-ion results are modified in two ways, both by setting $\theta\rightarrow\theta-\theta_{1,1}$ and $\phi\rightarrow\phi-\phi_{1,1}-\psi_{1,1}-\pi/2$, but also by renormalizing J_e. To first order in J_e, $J_e\rightarrow J_e\cos(2\psi_{1,1})$.

2. Exact eigenvalues for $s_1=1/2$

For $s_1=1/2$, we let

$$x=\frac{J_c^2}{4}+\frac{J_f^2}{12}+b^2, \tag{A6}$$

$$y=\frac{J_f}{12}\left(J_c^2-\frac{J_f^2}{9}\right)+\frac{b^2}{2}\left[J_f\left(\frac{2}{3}-\sin^2\theta\right)+J_c\sin^2\theta\cos(2\phi)\right], \tag{A7}$$

$$A=\left[-\frac{y}{2}+i\sqrt{-\frac{y^2}{4}+\frac{x^3}{27}}\right]^{1/3}, \tag{A8}$$

where the argument of the square root is positive definite. Then, the exact real eigenvalues λ_n are given by

$$\lambda_n=2\,\mathrm{Re}(A),\quad -\mathrm{Re}(A)\pm\sqrt{3}\,\mathrm{Im}(A) \tag{A9}$$

for $n=2,3,4$.

3. Specific-heat details for $s_1=1/2$

We first present the numerators of the exact expressions for the specific heat with $s_1=1/2$ and $\boldsymbol{B}||\hat{\boldsymbol{i}}$ for $i=x,y,z$. We have

$$\mathcal{N}_{x,y}=F_{x,y}^2+\frac{1}{4}(J+2J_{y,x})^2e^{\beta[2(J_{y,x}-J_{x,y})-J]}+F_{x,y}\sinh(\beta F_{x,y})e^{-\beta J_{x,y}}[(J+J_{x,y})e^{-\beta J}+(J_{x,y}-2J_{y,x})e^{2\beta J_{y,x}}]+\frac{1}{2}e^{-\beta J_{x,y}}\cosh(\beta F_{x,y})\{[(J+J_{x,y})^2+F_{x,y}^2]e^{-\beta J}+[(2J_{y,x}-J_{x,y})^2+F_{x,y}^2]e^{2\beta J_{y,x}}, \tag{A10}$$

$$\mathcal{N}_z=F_z^2\cosh(2\beta F_z)+\frac{J^2}{4}e^{-\beta(J+J_f)}+\frac{1}{2}\cosh(\beta F_z)\times\left[\Delta_z\left(\frac{J_f^2}{4}+F_z^2\right)+e^{-\beta(J+J_f/2)}J(J+J_f)\right]+F_z\sinh(\beta F_z)\left(\frac{J_f}{2}\Delta_z+Je^{-\beta(J+J_f/2)}\right). \tag{A11}$$

4. Eigenvalues for $s_1=1$ in the crystal representation

In the remainder of this appendix, we provide some details of our exact results for $s_1=1$. The cubic equation for the three $s=1$ eigenvalues is given by

$$\epsilon_n=-J-J_a+\lambda_n,\quad \text{for}\quad n=2,3,4, \tag{A12}$$

$$0=-\lambda_n^3-(J_a-J_f)\lambda_n^2+\lambda_n[b^2+(J_c-J_e)^2]+(J_a-J_f)\times[b^2\cos^2\theta+(J_c-J_e)^2]-(J_c-J_e)(b^2\sin^2\theta\cos(2\phi)). \tag{A13}$$

An exact solution for these triplet states are an arbitrary $\boldsymbol{B}$ may be found as for the $s_1=1/2$ dimer in Eqs. (A6)–(A9). For simplicity, we only list some special cases. For $\boldsymbol{B}=0$, we have

$$\lambda_n^0=-J_a+J_f,\pm(J_e-J_c), \tag{A14}$$

For $\boldsymbol{B}||\hat{\boldsymbol{z}}$,

$$\lambda_n=J_f-J_a,\pm\sqrt{b^2+(J_c-J_e)^2}. \tag{A15}$$

For $\boldsymbol{B}||\hat{\boldsymbol{x}},\hat{\boldsymbol{y}}$, we have

$$\lambda_n=\pm(J_e-J_c),-J_{y,x}\pm\sqrt{b^2+\bar{J}_{x,y}^2}, \tag{A16}$$

$$\bar{J}_{x,y}=\frac{1}{2}[J_a-J_f\mp(J_c-J_e)], \tag{A17}$$

where for the first eigenvalue, $+(-)$ corresponds to $\hat{\boldsymbol{x}}$, $(\hat{\boldsymbol{y}})$, and $\bar{J}_x$ $(\bar{J}_y)$ corresponds to the upper (lower) sign.

The six eigenvalues for the mixed $s=0,2$ states satisfy

$$\epsilon_n=-3J-\frac{4}{3}J_a-\frac{1}{3}J_f+\lambda_n. \tag{A18}$$

We first define

$$a=-\frac{\sqrt{2}}{3}(2J_a-J_f), \tag{A19}$$

$$b_\perp = -b \sin\theta e^{-i\phi}, \tag{A20}$$

$$b_3 = \sqrt{\frac{3}{2}} b_\perp, \tag{A21}$$

$$d = -\sqrt{\frac{2}{3}}(J_c + J_e), \tag{A22}$$

$$d_3 = \sqrt{\frac{3}{2}} d, \tag{A23}$$

$$e = -\frac{1}{\sqrt{3}}(2J_e - J_c), \tag{A24}$$

$$\tilde{J} = J - \frac{1}{9}(2J_a - J_f), \tag{A25}$$

and

$$Q_n^p = \frac{n}{3}(J_f + J_a) + pb\cos\theta. \tag{A26}$$

Then the λ_n are the eigenvalues of the Hermitian matrix $\overleftrightarrow{M}$ given by

$$\overleftrightarrow{M} = \begin{pmatrix} Q_{-2}^{-2} & b_\perp & d & 0 & 0 & e \\ b_\perp^* & Q_1^{-1} & b_3 & d_3 & 0 & 0 \\ d & b_3^* & Q_2^0 & b_3 & d & a \\ 0 & d_3 & b_3^* & Q_1^1 & b_\perp & 0 \\ 0 & 0 & d & b_\perp^* & Q_{-2}^2 & e \\ e & 0 & a & 0 & e & Q_2^0 + 3\tilde{J} \end{pmatrix}. \tag{A27}$$

The resulting sixth order polynomial for the λ_n is given elsewhere.[61] We note that for $\boldsymbol{B}||\hat{\boldsymbol{i}}$, $\overleftrightarrow{M}$ is block diagonal, breaking up into matrices of ranks 2 and 4. These cases are discussed in detail elsewhere.[61] Here we only present the simplest data for which the eigenvalues are determined either by linear or by quadratic equations.

5. Simple special $s_1=1$ cases

When only one of the $J_j \neq 0$, the eigenvalues for $\boldsymbol{B}||\hat{z}$ simplify considerably. For $J_f \neq 0$, we have

$$\lambda_n^z = 3J + J_f, J_f, J_f/2 \pm b, -J_f \pm 2b. \tag{A28}$$

For $J_c \neq 0$, we find

$$\lambda_n^z = 0, 3J, \pm\sqrt{b^2 + 9J_c^2/4}, \pm\sqrt{4b^2 + 3J_c^2}. \tag{A29}$$

For $J_a - J_f/2 \neq 0$, the eigenvalues can also be found analytically,

$$\lambda_n^z = -\frac{2J_a - J_f}{3} \pm 2b, \frac{2J_a - J_f}{6} \pm b, \frac{2J_a - J_f}{6} + \frac{3J}{2} \pm \frac{1}{2}\sqrt{9J^2 + (2J_a - J_f)^2 - 2J(2J_a - J_f)}. \tag{A30}$$

We note that the ground state energy in this case is

$$E_1 = -\frac{(3J - J_f)}{2} - J_a - \frac{1}{2}\sqrt{9J^2 + (2J_a - J_f)^2 - 2J(2J_a - J_f)}, \tag{A31}$$

which explicitly involves mixing of the $s=m=0$ and the $s=2, m=0$ states.

At the first level crossing with $\boldsymbol{B}||\hat{z}$, we have for $J_a - J_f/2 \neq 0$ and the other $J_j = 0$,

$$\gamma B_{1,1}^{\mathrm{lc},z} = \frac{1}{2}\{J + [9J^2 + (2J_a - J_f)^2 - 2J(2J_a - J_f)]^{1/2}\}. \tag{A32}$$

We note that the first level crossing for J_c, $J_f \neq 0$ for $\boldsymbol{B}\|\hat{\boldsymbol{i}}$ is equivalent to that of $s_1 = 1/2$, given by Eq. (64). At the second level crossing, simple formulas are only obtained for $\boldsymbol{B}\|\hat{z}$ with one $J_j \neq 0$. For $\boldsymbol{B}\|\hat{z}$ and $J_a \neq 0$, $J_f \neq 0$, and $J_c \neq 0$, respectively, we have

$$\gamma B_{2,1}^{\mathrm{lc},z} = \begin{cases} -2J - J_a, \\ -2J - 3J_f/2, \\ \frac{1}{3}(20J^2 - 15J_c^2/2 + 8[4J^4 - 3J^2J_c^2/2]^{1/2})^{1/2}. \end{cases} \tag{A33}$$

APPENDIX B

1. Rotation to the induction representation

The rotation from the crystal representation to the induction representation is obtained from

$$\begin{pmatrix} \hat{\boldsymbol{x}} \\ \hat{\boldsymbol{y}} \\ \hat{\boldsymbol{z}} \end{pmatrix} = \begin{pmatrix} \cos\theta\cos\phi & -\sin\phi & \sin\theta\cos\phi \\ \cos\theta\sin\phi & \cos\phi & \sin\theta\sin\phi \\ -\sin\theta & 0 & \cos\theta \end{pmatrix} \begin{pmatrix} \hat{\boldsymbol{x}}' \\ \hat{\boldsymbol{y}}' \\ \hat{\boldsymbol{z}}' \end{pmatrix}, \tag{B1}$$

leading to $\boldsymbol{B} = B\hat{\boldsymbol{z}}'$.[70] This operation is equivalent to a rotation by $-\pi/2$ about the uniaxial anisotropy z axis, a rotation by θ about the transformed x axis, and then a rotation by $\pi/2 - \phi$ about the transformed z axis.[69] In effect, in using the above rotation matrix, we made the arbitrary choice that the rotated z axis lies in the $x'z'$ plane. After the above rotation, it is still possible to rotate the crystal by an arbitrary angle ζ about the z' axis, keeping $\boldsymbol{B}\|\hat{\boldsymbol{z}}'$. Hence there are in effect an infinite number of equivalent rotations leading to $\boldsymbol{B} = B\hat{\boldsymbol{z}}'$. The resulting Hamiltonian matrix will then have off-diagonal elements that depend upon ζ. However, all such rotations

necessarily lead to the identical, ζ-independent, set of eigenvalues of the resulting diagonalized Hamiltonian matrix. We have explicitly checked that the above rotation gives the exact cubic expression, Eq. (54), for the $s_1=1/2$ eigenvalues, and also leads to the correct eigenstate energies second order in each of the J_j for $s_1=1$. We also showed explicitly that ζ does not enter the eigenstate energies second order in J_f for arbitrary s,s_1,m.

2. Second-order induction representation Hamiltonian

In this section, we evaluate the corrections to the eigenstate energies second order in the four anisotropy interaction energies J_j for $j=a,c,e,f$. The operations of the induction representation Hamiltonian $\tilde{\mathcal{H}}'$ upon the eigenstates $|\varphi_s^m\rangle$ may be written as

$$\tilde{\mathcal{H}}'|\varphi_s^m\rangle = (E_s^{m,(0)} + E_{s,s_1}^{m,(1)})|\varphi_s^m\rangle + \sum_{\sigma'=\pm 1} \mathcal{W}_{s,s_1}^{m,\sigma'}|\varphi_{s+2\sigma'}^m\rangle + \sum_{\sigma=\pm 1} (\mathcal{U}_{s,s_1}^{m,\sigma}|\varphi_s^{m+\sigma}\rangle + \mathcal{V}_{s,s_1}^{m,\sigma}|\varphi_s^{m+2\sigma}\rangle) + \sum_{\sigma,\sigma'=\pm 1} (\mathcal{X}_{s,s_1}^{m,\sigma,\sigma'}|\varphi_{s+2\sigma'}^{m+\sigma}\rangle + \mathcal{Y}_{s,s_1}^{m,\sigma,\sigma'}|\varphi_{s+2\sigma'}^{m+2\sigma}\rangle), \tag{B2}$$

where $E_{s,s_1}^{m,(0)}$ and $E_{s,s_1}^{m,(1)}$ are given by Eqs. (46) and (47), respectively, and

$$\mathcal{U}_{s,s_1}^{m,\sigma}(\theta,\phi) = \frac{1}{4}(2m+\sigma)A_s^{\sigma m}\{\sin(2\theta)[\tilde{J}_{f,a}^{s,s_1} - \tilde{J}_{c,e}^{s,s_1}\cos(2\phi)] - 2i\sigma\tilde{J}_{c,e}^{s,s_1}\sin\theta\sin(2\phi)\}, \tag{B3}$$

$$\mathcal{V}_{s,s_1}^{m,\sigma}(\theta,\phi) = -\frac{1}{4}F_s^{\sigma m}[\tilde{J}_{f,a}^{s,s_1}\sin^2\theta + \tilde{J}_{c,e}^{s,s_1}(1+\cos^2\theta)\cos(2\phi) + 2i\sigma\tilde{J}_{c,e}^{s,s_1}\cos\theta\sin(2\phi)], \tag{B4}$$

$$\mathcal{W}_{s,s_1}^{m,\sigma'}(\theta,\phi) = -\frac{1}{4}H_{s,s_1}^{m,\sigma'}[(2J_a - J_f)\cos^2\theta + (2J_e - J_c)\sin^2\theta\cos(2\phi)] + \frac{1}{16}N_{s,s_1}^{m,\sigma'}\sin^2\theta[2J_a - J_f - (2J_e - J_c)\cos(2\phi)], \tag{B5}$$

$$\mathcal{X}_{s,s_1}^{m,\sigma,\sigma'}(\theta,\phi) = -\frac{\sigma\sigma'}{16}R_{s,s_1}^{m,\sigma,\sigma'}\{\sin(2\theta)[2J_a - J_f - (2J_e - J_c)\cos(2\phi)] - i\sigma(2J_e - J_c)\sin\theta\sin(2\phi)\}, \tag{B6}$$

and

$$\mathcal{Y}_{s,s_1}^{m,\sigma,\sigma'}(\theta,\phi) = -\frac{1}{16}K_{s,s_1}^{\sigma m,\sigma'}\{(2J_a - J_f)\sin^2\theta + (2J_e - J_c)[(1+\cos^2\theta)\cos(2\phi) + 2i\sigma\cos\theta\sin(2\phi)]\}, \tag{B7}$$

where

$$N_{s,s_1}^{m,\sigma'} = \sum_{\sigma=\pm 1} C_{s+(\sigma'+1)/2,s_1}^{-\sigma\sigma' m-(\sigma'+1)/2} C_{s+(3\sigma'+1)/2,s_1}^{\sigma\sigma' m+(\sigma'-1)/2}, \tag{B8}$$

$$R_{s,s_1}^{m,\sigma,\sigma'} = C_{s+(\sigma'+1)/2,s_1}^{-m\sigma\sigma'-(\sigma'+1)/2} D_{s+(3\sigma'+1)/2,s_1}^{m+\sigma} + C_{s+(3\sigma'+1)/2,s_1}^{-m\sigma\sigma'-(\sigma'+1)/2} D_{s+(\sigma'+1)/2,s_1}^{m}, \tag{B9}$$

and η_{s,s_1}, G_{s,s_1}^m, $H_{s,s_1}^{m,\sigma'}$, $K_{s,s_1}^{x,\sigma'}$, and L_{s,s_1}^x are given by Eqs. (22) and (25)–(28), respectively. We note that for $\sigma'=\pm 1$, $N_{s,s_1}^{m,\sigma'} = 2H_{s,s_1}^{m,\sigma'}$.

3. Second-order eigenstate energies

From Eq. (B2), the second-order eigenstate energies may be written as

$$E_{s,s_1}^{m,(2)} = \frac{1}{\gamma B}\sum_{\sigma=\pm 1}\sigma\left(|\mathcal{U}_{s,s_1}^{m,\sigma}|^2 + \frac{1}{2}|\mathcal{V}_{s,s_1}^{m,\sigma}|^2\right) + \sum_{\sigma'=\pm 1}\frac{|\mathcal{W}_{s,s_1}^{m,\sigma'}|^2}{J[2+(2s+1)\sigma']} + \sum_{\sigma,\sigma'\pm 1}\left(\frac{|\mathcal{X}_{s,s_1}^{m,\sigma,\sigma'}|^2}{J[2+(2s+1)\sigma'] + \sigma\gamma B} + \frac{|\mathcal{Y}_{s,s_1}^{m,\sigma,\sigma'}|^2}{J[2+(2s+1)\sigma'] + 2\sigma\gamma B}\right). \tag{B10}$$

For simplicity, we rewrite this as

$$E_{s,s_1}^{m,(2)} = E_{s,s_1}^{m,(2)\mathcal{U}} + E_{s,s_1}^{m,(2)\mathcal{V}} + E_{s,s_1}^{m,(2)\mathcal{W}} + E_{s,s_1}^{m,(2)\mathcal{X}} + E_{s,s_1}^{m,(2)\mathcal{Y}}, \tag{B11}$$

$$E_{s,s_1}^{m,(2)\mathcal{U}} = \frac{m\sin^2\theta}{2\gamma B}[4s(s+1) - 8m^2 - 1] \times\{\cos^2\theta[\tilde{J}_{f,a}^{s,s_1} - \cos(2\phi)\tilde{J}_{c,e}^{s,s_1}]^2 + \sin^2(2\phi)(\tilde{J}_{c,e}^{s,s_1})^2\}, \tag{B12}$$

$$E_{s,s_1}^{m,(2)\mathcal{V}} = -\frac{m}{8\gamma B}[2s(s+1) - 2m^2 - 1]\times\{[\sin^2\theta\tilde{J}_{f,a}^{s,s_1} + (1+\cos^2\theta)\cos(2\phi)\tilde{J}_{c,e}^{s,s_1}]^2 + 4\cos^2\theta\sin^2(2\phi)(\tilde{J}_{c,e}^{s,s_1})^2\}, \tag{B13}$$

$$E^{m,(2)\mathcal{W}}_{s,s_1} = \frac{d^m_{s,s_1}}{32J}\{(2J_a - J_f)(1 - 3\cos^2\theta) - 3(2J_e - J_c)\sin^2\theta\cos(2\phi)]^2, \tag{B14}$$

$$E^{m,(2)\mathcal{X}}_{s,s_1} = \frac{f^m_{s,s_1}(\gamma B/J)\sin^2\theta}{4J} \times \{[2J_a - J_f - (2J_e - J_c)\cos(2\phi)]^2\cos^2\theta + \sin^2(2\phi)(2J_e - J_c)^2\}, \tag{B15}$$

$$E^{m,(2)\mathcal{Y}}_{s,s_1} = \frac{g^m_{s,s_1}(\gamma B/J)}{128J}\{[(2J_a - J_f)\sin^2\theta + (2J_e - J_c)(1 + \cos^2\theta)\cos(2\phi)]^2 + 4\cos^2\theta\sin^2(2\phi)(2J_e - J_c)^2\}, \tag{B16}$$

where

$$d^m_{s,s_1} = -\frac{(s^2 - m^2)[(s-1)^2 - m^2]\eta^2_{s,s_1}\eta^2_{s-1,s_1}}{(2s-1)} + \eta^2_{s+2,s_1}\eta^2_{s+1,s_1}\frac{[(s+1)^2 - m^2][(s+2)^2 - m^2]}{(2s+3)}, \tag{B17}$$

$$f^m_{s,s_1}(x) = -\frac{\eta^2_{s,s_1}\eta^2_{s-1,s_1}(s^2 - m^2)}{(2s-1)^2 - x^2}\{(2s-1)[(s-1)(s-2) + m^2] - m(2s-3)x\} + \frac{\eta^2_{s+2,s_1}\eta^2_{s+1,s_1}[(s+1)^2 - m^2]}{(2s+3)^2 - x^2}\{(2s+3) \times [(s+2)(s+3) + m^2] - m(2s+5)x\}, \tag{B18}$$

$$g^m_{s,s_1}(x) = -\frac{2\eta^2_{s,s_1}\eta^2_{s-1,s_1}}{(2s-1)^2 - 4x^2}\{(2s-1)[m^4 + m^2(6s^2 - 18s + 11) + s(s-1)(s-2)(s-3)] - 4mx(2s-3)(s^2 - 3s + 1 + m^2)\} + \frac{2\eta^2_{s+2,s_1}\eta^2_{s+1,s_1}}{(2s+3)^2 - 4x^2}\{(2s+3)[m^4 + m^2(6s^2 + 30s + 35) + (s+1)(s+2)(s+3)(s+4)] - 4mx(2s+5) \times (s^2 + 5s + 5 + m^2)\}. \tag{B19}$$

There is a remarkable amount of symmetry in the angular dependence of the eigenstate energies. We note that $E^{m,(2)\mathcal{X}}_{s,s_1}(\theta,\phi)$ and $E^{m,(2)\mathcal{U}}_{s,s_1}(\theta,\phi)$ have the same forms, differing in the replacements of the interactions $\tilde{J}^{s,s_1}_{f,a}$ and $\tilde{J}^{s,s_1}_{c,e}$ with $2J_a - J_f$ and $2J_e - J_c$, respectively, and with different overall constant functions. The same comparison can also be made with $E^{m,(2)\mathcal{Y}}_{s,s_1}(\theta,\phi)$ and $E^{m,(2)\mathcal{V}}_{s,s_1}(\theta,\phi)$. In addition, we note that there is a remarkable similarity in the θ,ϕ dependence of $E^{m,(2)\mathcal{W}}_{s,s_1}$ with that of the local spin anisotropy part of $B^{\mathrm{lc}(1)}_{s,s_1} \times(\theta,\phi)$given by Eq. (50).

4. Second-order level crossing angular functions

The angular functions $f^{(2)}_n(\theta,\phi)$ in Eq. (50) are

$$f^{(2)}_1(\theta,\phi) = \frac{\sin^2\theta}{4J^2}\{[J_f - \cos(2\phi)J_c]^2\cos^2\theta + J_c^2\sin^2(2\phi)\}, \tag{B20}$$

$$f^{(2)}_2(\theta,\phi) = \frac{\sin^2\theta}{4J^2}\{\cos^2\theta[J_f - J_c\cos(2\phi)][2J_a - J_f - (2J_e - J_c)\cos(2\phi)] + [J_c(2J_e - J_c)\sin^2(2\phi)]\}, \tag{B21}$$

$$f^{(2)}_3(\theta,\phi) = \frac{\sin^2\theta}{4J^2}\{[2J_a - J_f - \cos(2\phi)(2J_e - J_c)]^2\cos^2\theta + (2J_e - J_c)^2\sin^2(2\phi)\}, \tag{B22}$$

$$f^{(2)}_4(\theta,\phi) = \frac{1}{4J^2}[J_f\sin^2\theta + J_c(1 + \cos^2\theta)\cos(2\phi)]^2 + \frac{J_c^2}{J^2}\cos^2\theta\sin^2(2\phi), \tag{B23}$$

$$f^{(2)}_5(\theta,\phi) = \frac{1}{4J^2}[J_f\sin^2\theta + J_c(1 + \cos^2\theta)\cos(2\phi)] \times [(2J_a - J_f)\sin^2\theta + (2J_e - J_c)(1 + \cos^2\theta)\cos(2\phi)] + \frac{J_c(2J_e - J_c)}{J^2}\cos^2\theta\sin^2(2\phi), \tag{B24}$$

$$f^{(2)}_6(\theta,\phi) = \frac{1}{4J^2}[(2J_a - J_f)\sin^2\theta + (2J_e - J_c)(1 + \cos^2\theta)\cos(2\phi)]^2 + \frac{(2J_e - J_c)^2}{J^2}\cos^2\theta\sin^2(2\phi), \tag{B25}$$

$$f^{(2)}_7(\theta,\phi) = \frac{1}{4J^2}\{(2J_a - J_f)(1 - 3\cos^2\theta) - 3(2J_e - J_c)\sin^2\theta\cos(2\phi)]^2. \tag{B26}$$

5. Second-order level crossing coefficients

The coefficients $a_n(s,s_1)$ in Eq. (50) are

$$a_1(s,s_1) = \frac{(9 - 20s + 12s^2)}{2s}, \tag{B27}$$

$$a_2(s,s_1) = \frac{[a_{2,0}(s) + 4s_1(s_1+1)a_{2,1}(s)]}{s(2s+1)(2s+3)}, \tag{B28}$$

$$a_{2,0}(s) = 3(9 + s - 23s^2 + 4s^3 + 12s^4), \tag{B29}$$

$$a_{2,1}(s) = 9 - 8s - 4s^2, \tag{B30}$$

$$a_3(s,s_1) = a_3^{\mathcal{U}}(s,s_1) + a_3^{\mathcal{X}}(s,s_1), \tag{B31}$$

$$a_3^{\mathcal{U}}(s,s_1) = \frac{[3-3s-3s^2+4s_1(s_1+1)]^2}{2(2s+3)^2} - \frac{(s-1)[3+3s-3s^2+4s_1(s_1+1)]^2}{2s(2s+1)^2}, \tag{B32}$$

$$a_3^{\mathcal{X}}(s,s_1) = \frac{[s(s+2)-4s_1(s_1+1)]}{2(s+1)(s+3)(2s+1)^2(2s+3)^2} \times \left(\frac{a_{3,0}^{\mathcal{X}}(s) + 4s_1(s_1+1)a_{3,1}^{\mathcal{X}}(s)}{(2s+5)(3s+1)} \right), \tag{B33}$$

$$a_{3,0}^{\mathcal{X}}(s) = (s+1)(s+3)(51+114s+209s^2+302s^3+164s^4 + 24s^5), \tag{B34}$$

$$a_{3,1}^{\mathcal{X}}(s) = 129+318s+395s^2+442s^3+300s^4+72s^5, \tag{B35}$$

$$a_4(s,s_1) = \frac{(4s-3)}{8s}, \tag{B36}$$

$$a_5(s,s_1) = -\frac{3[a_{5,0}(s)+4s_1(s_1+1)]}{4s(2s+1)(2s+3)}, \tag{B37}$$

$$a_{5,0}(s) = 3+3s-5s^2-4s^3, \tag{B38}$$

$$a_6(s,s_1) = a_6^{\mathcal{Y}}(s,s_1) + a_6^{\mathcal{Y}}(s,s_1), \tag{B39}$$

$$a_6^{\mathcal{Y}}(s,s_1) = \frac{[3-3s-3s^2+4s_1(s_1+1)]^2}{8(2s-1)(2s+3)^2} - \frac{(s-1)[3+3s-3s^2+4s_1(s_1+1)]^2}{8s(2s-3)(2s+1)^2}, \tag{B40}$$

$$a_6^{\mathcal{Y}}(s,s_1) = \frac{1}{4(2s-3)(2s-1)(2s+1)^2(2s+3)^2} \times \left(\frac{\sum_{n=0}^{2} a_{6,n}^{\mathcal{Y}}(s)[4s_1(s_1+1)]^n}{(2s+5)(4s+1)(4s+3)} \right), \tag{B41}$$

$$a_{6,0}^{\mathcal{Y}}(s) = s(-216+837s+5052s^2+3521s^3-12414s^4 - 21876s^5-7464s^6+6720s^7+5376s^8+1024s^9), \tag{B42}$$

$$a_{6,1}^{\mathcal{Y}}(s) = 3(81+102s+10s^2+196s^3+296s^4+80s^5), \tag{B43}$$

$$a_{6,2}^{\mathcal{Y}}(s) = 189+258s-100s^2+152s^3+640s^4+256s^5, \tag{B44}$$

$$a_7(s,s_1) = \frac{[s(s+2)-4s_1(s_1+1)]}{4(2s+1)^3(2s+3)^3(2s+5)}[4s_1(s_1+1)(-1+38s + 60s^2+24s^3) + (s+1)(3+67s+94s^2+44s^3 + 8s^4)]. \tag{B45}$$

By expanding the solutions in the crystal representation to second order in the J_j, we have explicitly checked these expressions for $s_1=1/2, s=1$, and for $s_1=1$, $s=1,2$. We note that for $s_1=1/2$, only a_1 and a_4 are nonvanishing.

6. Two-level thermodynamic coefficients $a_{1,s}$

Here we present the expression for $a_{1,s}$ to $\mathcal{O}(J_j/J)^2$ appearing in Eqs. (39) and (41)–(44) in the text. We have

$$a_{1,s} = s + \sum_{n=1}^{6} b_n(s,s_1) f_n^{(2)}(\theta,\phi) + \mathcal{O}(J_j/J)^3, \tag{B46}$$

where the $f_n(\theta,\phi)$ are given by Eqs. (B20)–(B25), and

$$b_1(s,s_1) = \frac{(2s-1)^2}{2s}\Theta(s-1), \tag{B47}$$

$$b_2(s,s_1) = \frac{(2s-1)^2}{s}\alpha_{s,s_1}\Theta(s-1), \tag{B48}$$

$$b_3(s,s_1) = \frac{(2s-1)^2}{2s}\alpha_{s,s_1}^2\Theta(s-1) + b_3^{\mathcal{X}}(s,s_1), \tag{B49}$$

$$b_3^{\mathcal{X}}(s,s_1) = -\frac{s(27+44s+27s^2+6s^3)}{6(s+1)^2(s+3)^2(2s+3)^2(2s+5)} \times \{[4s_1(s_1+1)-s(s+2)] \times [4s_1(s_1+1)-(s+1)(s+3)]\}, \tag{B50}$$

$$b_4(s,s_1) = \frac{(2s-1)}{8s}\Theta(s-1), \tag{B51}$$

$$b_5(s,s_1) = \frac{(2s-1)}{4s}\alpha_{s,s_1}\Theta(s-1), \tag{B52}$$

$$b_6(s,s_1) = \frac{(2s-1)}{8s}\alpha_{s,s_1}^2\Theta(s-1) + b_6^{\mathcal{Y}}(s,s_1), \tag{B53}$$

$$b_6^{\mathcal{Y}}(s,s_1) = \frac{s(s-1)}{8(4s^2-1)}[s^2-1-4s_1(s_1+1)] \times [s(s-2)-4s_1(s_1+1)] - \frac{sb_{6,1}(s)[s(s+2)-4s_1(s_1+1)]}{72(2s+1)(2s+3)^2(2s+5)(4s+3)^2} \times [(s+1)(s+3)-4s_1(s_1+1)], \quad \text{(B54)}$$

$$b_{6,1}(s) = 369 + 1011s + 1420s^2 + 1076s^3 + 416s^4 + 64s^5, \quad \text{(B55)}$$

where $\Theta(x)=1$ for $x\geq 0$, $\Theta(x)=0$ for $x<0$ is the Heaviside step function.

7. Higher-order EPR coefficients

Here we list the coefficients of the ten additional EPR resonances In Eq. (80). The first resonance has $a_1=1/2$, $b_1=2(m+\sigma)$, and $c_1=0$. The second resonance has $a_2=1$, $b_2=(2m-\sigma)/2$, and $c_2=0$. The next two resonances have $a_3=1$, $b_{3\pm}=\sigma[2\pm\sigma(2s+1)]$, and $c_3=-(2m+\sigma)/2$. The fifth and sixth resonances have $a_4=2$, $b_{4\pm}=2\sigma[2\pm\sigma(2s+1)]$, and $c_4=4(m+\sigma)$. Resonances 7–10 can be written using $\sigma',\sigma''=\pm\sigma$, and have $a_{5,\sigma'}=1/(1+2\sigma\sigma')$, $b_{5,\sigma',\sigma''}=[2+\sigma''(2s+1)]/(\sigma+2\sigma')$, and $c_{5,\sigma'}=m+\sigma'+\sigma/2$.

*Electronic address: efremov@theory.phy.tu-dresden.de
†Electronic address: klemm@phys.ksu.edu

[1] R. Sessoli, D. Gatteschi, A. Caneschi, and M. A. Novak, Nature (London) **365**, 141 (1993).
[2] J. R. Friedman, M. P. Sarachik, J. Tejada, and R. Ziolo, Phys. Rev. Lett. **76**, 3830 (1996).
[3] M. N. Leuenberger and D. Loss, Nature (London) **410**, 789 (2001).
[4] W. Wernsdorfer, T. Ohm, C. Sangregorio, R. Sessoli, D. Mailly, and C. Paulsen, Phys. Rev. Lett. **82**, 3903 (1999).
[5] W. Wernsdorfer and R. Sessoli, Science **284**, 133 (1999).
[6] D. Zipse, J. M. North, N. S. Dalal, S. Hill, and R. S. Edwards, Phys. Rev. B **68**, 184408 (2003).
[7] M. Affronte, A. Cornia, A. Lascialfari, F. Borsa, D. Gatteschi, J. Hinderer, M. Horvatić, A. G. M. Jansen, and M.-H. Julien, Phys. Rev. Lett. **88**, 167201 (2002).
[8] O. Waldmann, J. Schülein, R. Koch, P. Müller, I. Bernt, R. W. Saalfrank, H. P. Andres, H. U. Güdel, and P. Allenspach, Inorg. Chem. **38**, 5879 (1999).
[9] O. Waldmann, R. Koch, S. Schromm, J. Schülein, P. Müller, I. Bernt, R. W. Saalfrank, F. Hempel, and E. Balthes, Inorg. Chem. **40**, 2986 (2001).
[10] H. Nakano and S. Miyashita, J. Phys. Chem. Solids **63**, 1519 (2002).
[11] A. Cornia, M. Affronte, A. G. M. Jansen, G. L. Abbati, and D. Gatteschi, Angew. Chem., Int. Ed. **38**, 2264 (1999).
[12] A. Cornia, A. G. M. Jansen, and M. Affronte, Phys. Rev. B **60**, 12177 (1999).
[13] K. L. Taft, C. D. Delfs, G. C. Papaefthymiou, S. Foner, D. Gatteschi, and S. J. Lippard, J. Am. Chem. Soc. **116**, 823 (1994).
[14] O. Waldmann, T. Guidi, S. Carretta, C. Mondelli, and A. L. Dearden, Phys. Rev. Lett. **91**, 237202 (2003).
[15] S. Carretta, J. van Slageren, T. Guidi, E. Liviotti, C. Mondelli, D. Rovai, A. Cornia, A. L. Dearden, F. Carsughi, M. Affronte, C. D. Frost, R. E. P. Winpenny, D. Gatteschi, G. Amoretti, and R. Caciuffo, Phys. Rev. B **67**, 094405 (2003).
[16] S. Carretta, P. Santini, G. Amoretti, M. Affronte, A. Ghirri, I. Sheikin, S. Piligkos, G. Timco, and R. E. P. Winpenny, Phys. Rev. B **72**, 060403(R) (2005).
[17] O. Waldmann, J. Schülein, R. Koch, P. Müller, I. Bernt, R. W. Saalfrank, H. P. Andres, H. U. Güdel, and P. Allenspach, Inorg. Chem. **38**, 5879 (1999).
[18] O. Waldmann, R. Koch, S. Schromm, J. Schülein, P. Müller, I. Bernt, R. W. Saalfrank, F. Hampel, and E. Balthes, Inorg. Chem. **40**, 2986 (2001).
[19] D. A. Tennant, S. E. Nagler, A. W. Garrett, T. Barnes, and C. C. Torardi, Phys. Rev. Lett. **78**, 4998 (1997).
[20] A. Furrer and H. U. Güdel, Phys. Rev. Lett. **39**, 657 (1977).
[21] H. U. Güdel, Neutron News **7**, 24 (1996).
[22] A. W. Garrett, S. E. Nagler, D. A. Tennant, B. C. Sales, and T. Barnes, Phys. Rev. Lett. **79**, 745 (1997).
[23] C. Mennerich, H.-H. Klauss, M. Broekelmann, F. J. Litterst, C. Golze, R. Klingeler, V. Kataev, B. Büchner, S.-N. Grossjohann, W. Brenig, M. Goiran, H. Rakoto, J.-M. Broto, O. Kataeva, and D. J. Price, Phys. Rev. B **73**, 174415 (2006).
[24] B. Grenier, Y. Inagaki, L. P. Regnault, A. Wildes, T. Asano, Y. Ajiro, E. Lhotel, C. Paulsen, T. Ziman, and J. P. Boucher, Phys. Rev. Lett. **92**, 177202 (2004).
[25] Y. Inagaki, Ph.D. thesis, Kyushu University, Fukuoka, Japan, 2003.
[26] D. V. Efremov and R. A. Klemm, Phys. Rev. B **66**, 174427 (2002).
[27] F. Le Gall, F. Fabrizi de Biani, A. Caneschi, P. Cinelli, A. Cornia, A. C. Fabretti, and D. Gatteschi, Inorg. Chim. Acta **262**, 123 (1997).
[28] Y. Shapira, M. T. Liu, S. Foner, R. J. Howard, and W. H. Armstrong, Phys. Rev. B **63**, 094422 (2001).
[29] Y. Shapira, M. T. Liu, S. Foner, C. E. Dubé, and P. J. Bonitatebus, Jr., Phys. Rev. B **59**, 1046 (1999).
[30] V. A. Grillo, G. R. Hanson, D. Wang, T. W. Hambley, L. R. Gahan, K. S. Murray, B. Moubaraki, and C. J. Hawkins, Inorg. Chem. **35**, 3568 (1996).
[31] J. D. Walker and R. Poli, Inorg. Chem. **29**, 756 (1990).
[32] J. A. Bertrand, J. L. Breece, and P. G. Eller, Inorg. Chem. **13**, 125 (1974).
[33] L. E. Roy and T. Hughbanks, J. Am. Chem. Soc. **128**, 568 (2006).
[34] S. Liu, L. Gelmini, S. J. Rettig, R. C. Thompson, and C. Orvig, J. Am. Chem. Soc. **114**, 6081 (1992).
[35] S. T. Hatscher and W. Urland, Angew. Chem., Int. Ed. **42**, 2862 (2003).
[36] R. Tiron, W. Wernsdorfer, D. Foguet-Albiol, N. Aliaga-Alcalde, and G. Christou, Phys. Rev. Lett. **91**, 227203 (2003).

[37] J. M. North, N. S. Dalal, D. Foguet-Albiol, A. Vinslava, and G. Christou, Phys. Rev. B **69**, 174419 (2004).
[38] A. Sieber, D. Foguet-Albiol, O. Waldmann, S. T. Ochsenbein, R. Bircher, G. Christou, F. Fernandez-Alonso, H. Mutka, and H. U. Güdel, Inorg. Chem. **44**, 6771 (2005).
[39] A. Zheludev, Z. Honda, Y. Chen, C. L. Broholm, K. Katsumata, and S. M. Shapiro, Phys. Rev. Lett. **88**, 077206 (2002).
[40] A. Zheludev, Z. Honda, C. L. Broholm, K. Katsumata, S. M. Shapiro, A. Kolezhuk, S. Park, and Y. Qiu, Phys. Rev. B **68**, 134438 (2003).
[41] M. Hagiwara, L. P. Regnault, A. Zheludev, A. Stunault, N. Metoki, T. Suzuki, S. Suga, K. Kakurai, Y. Koike, P. Vorderwisch, and J.-H. Chung, Phys. Rev. Lett. **94**, 177202 (2005).
[42] Y. Chen, Z. Honda, A. Zheludev, C. Broholm, K. Katsumata, and S. M. Shapiro, Phys. Rev. Lett. **86**, 1618 (2001).
[43] Z. Honda, H. Asakawa, and K. Katsumata, Phys. Rev. Lett. **81**, 2566 (1998).
[44] We note that the term homonuclear is usually used in place of homoionic, but that is not precise, because a homonuclear dimer such as ^{55}Mn(II)^{55}Mn(III) is not homoelectronic, but contains two different ionic spin values.
[45] M. Tinkham, *Group Theory and Quantum Mechanics* (McGraw-Hill, New York, 1964).
[46] A. Bencini and D. Gatteschi, *Electron Paramagnetic Resonance of Exchange Coupled Systems* (Springer, Berlin, 1990).
[47] T. Moriya, Phys. Rev. **120**, 91 (1960); I. Dzyaloshinskii, J. Phys. Chem. Solids **4**, 241 (1958).
[48] O. Waldmann, J. Hassmann, P. Müller, D. Volkmer, U. S. Schubert, and J.-M. Lehn, Phys. Rev. B **58**, 3277 (1998).
[49] O. Waldmann and H. U. Güdel, Phys. Rev. B **72**, 094422 (2005).
[50] J. Schnack, M. Brüger, M. Luban, P. Kögerler, E. Morosan, R. Fuchs, R. Modler, H. Nojiri, R. C. Rai, J. Cao, J. L. Musfeldt, and X. Wei, Phys. Rev. B **73**, 094401 (2006).
[51] J. J. Borrás-Almenar, J. M. Clemente-Juan, E. Coronado, and B. S. Tsukerblat, Inorg. Chem. **38**, 6081 (1999).
[52] S. Carretta, E. Liviotti, N. Magnani, P. Santini, and G. Amoretti, Phys. Rev. Lett. **92**, 207205 (2004).
[53] R. Boča, *Theoretical Foundations of Molecular Magnetism* (Elsevier, New York, 1999).
[54] D. V. Efremov and R. A. Klemm (unpublished).
[55] R. A. Klemm and D. V. Efremov, cond-mat/0601591 (unpublished); cond-mat/0602417 (unpublished).
[56] J.-N. Rebilly, L. Catala, E. Rivière, R. Guillot, W. Wernsdorfer, and T. Mallah, Inorg. Chem. **44**, 8194 (2005).
[57] N. Aliaga-Alcalde, R. S. Edwards, S. O. Hill, W. Wernsdorfer, K. Folting, and G. Christou, J. Am. Chem. Soc. **126**, 12503 (2004).
[58] O. Waldmann, S. Carretta, P. Santini, R. Koch, A. G. M. Jansen, G. Amoretti, R. Caciuffo, L. Zhao, and L. K. Thompson, Phys. Rev. Lett. **92**, 096403 (2004).
[59] R. M. White, *Quantum Theory of Magnetism* (McGraw-Hill, New York, 1970), Chap. 1, 5, 8.
[60] R. A. Klemm, Phys. Rev. B **41**, 2073 (1990).
[61] D. V. Efremov and R. A. Klemm, cond-mat/0409168 (unpublished).
[62] A. Fetter and J. D. Walecka, *Quantum Theory of Many-Particle Systems* (McGraw-Hill, New York, 1971), p. 127.
[63] D. V. Efremov and R. A. Klemm (unpublished).
[64] S. Hill, J. A. A. J. Perenboom, N. S. Dalal, T. Hathaway, T. Stalcup, and J. S. Brooks, Phys. Rev. Lett. **80**, 2453 (1998).
[65] S. Hill, S. Maccagnano, K. Park, R. M. Achey, J. M. North, and N. S. Dalal, Phys. Rev. B **65**, 224410 (2002).
[66] S. Hill, R. S. Edwards, S. I. Jones, N. S. Dalal, and J. M. North, Phys. Rev. Lett. **90**, 217204 (2003).
[67] K. Park, M. A. Novotny, N. S. Dalal, S. Hill, and P. A. Rikvold, Phys. Rev. B **66**, 144409 (2002).
[68] B. Grenier (private communication).
[69] H. Goldstein, *Classical Mechanics* (Addison-Wesley, Reading, MA, 1965), p. 109.
[70] R. A. Klemm and J. R. Clem, Phys. Rev. B **21**, 1868 (1980); R. A. Klemm, SIAM J. Appl. Math. **55**, 986 (1995).